XMM-NEWTON OBSERVATIONS OF TOOTHBRUSH CLUSTER OF GALAXIES

by

Sinancan Kara

B.S., Physics, Boğaziçi University, 2016

Submitted to the Institute for Graduate Studies in
Science and Engineering in partial fulfillment of
the requirements for the degree of
Master of Science

Graduate Program in Physics
Boğaziçi University

2019

Fazilet ve Hürol Kara'ya

ACKNOWLEDGEMENTS

I would like to express my gratitude towards several of people for their support and help during my Msc.

I am very thankful to my supervisor Prof. Nihal Ercan for her constant support and guidance during not only my master thesis but also during both my Bs. and Msc. She opened so many doors for me and without her inspiration and encouragement this thesis would not be possible.

Also, I owe my appreciation to Ayşegül Tümer (very-soon-to-be Dr.) for her continuous help during my thesis, she helped me whenever I was in difficulty. I would also like to thank Mustafa Bozkurt for introducing me galaxy clusters and data analysis.

I offer my sincerest gratitude to Cansu Bilgici for her endless support which makes the impossible possible, thank you.

I would also like to thank my friends for being there for almost a decade; Gökhan Yalnız, Aytaç Paçal, Mert Ergen, Olcayto Alp Külünkoğlu, Sevdenur Arpacı and Dorukhan Salepçi. Also, many thanks to the cats JLo and Fermat for being joyful. I am sure that I forgot many people that I should have been thankful.

I thank my family for their continuous love and support. Without their guidance I would not be the person I am today. Thank you for buying so many books on space when I was a child, I dedicate this thesis to you.

I would like to thank TUBITAK for financial support through a 1002 project under the code 118F023.

ABSTRACT

XMM-NEWTON OBSERVATIONS OF TOOTHBRUSH CLUSTER OF GALAXIES

Clusters of galaxies are the largest gravitationally bound systems in the Universe. Their immense gravitational potential holds 10's to 100's bright galaxies and also an intracluster medium (ICM) surrounding them. ICM gets enriched by supernova explosions and is heated up to the temperatures of 10^7 to 10^8 K by the gravitational potential well, which causes X-ray emission.

The merging cool-core cluster 1RXSJ0603.3+4213 (z=0.225) shows a large radio relic associated with a merger shock north of its core. Because the shape of the radio relic is similar to a toothbrush, the cluster is nicknamed as "Toothbrush". Our aim is to investigate the metal abundance and produce a temperature map by using 82 ks X-ray observation of XMM-Newton in order to find how the shock affects parameters radially.

ÖZET

TOOTHBRUSH GALAKSİ KÜMESİNİN XMM-NEWTON GÖZLEMLERİ

Kütle çekimi sayesinde evrende bir arada duran en büyük yapılar galaksi kümeleridir. Çok büyük olan kütle çekimleri onlarcadan yüzlerceye parlak galaksiyi ve bu galaksileri saran küme içi gazı (KİG) bir arada tutar. KİG süpernova patlamaları sayesinde zenginleşir ve kütleçekim potansiyeli sayesinde 10^7 ile 10^8 K arası sıcaklığa ulaşır, bu da X-ışını yaymasına sebep olur.

Birleşen soğuk-çekirdekli 1RXSJ0603.3+4213 (z=0.225) kümesi çekirdeğinin kuzeyinde birleşimin sebep olduğu bir radyo kalıntısı göstermektedir. Bu radyo kalıntısının şekli bir diş fırçasına benzediğinden küme "Diş Fırçası (Toothbrush)" takma adını almıştır. Amacımız XMM-Newton'dan alınan 82 ks X-ışın gözlemini inceleyerek metal bolluğu sıcaklık haritası çıkartmak ve böylece şok dalgasının bu parametreleri nasıl etkilediğini bulmaktır.

TABLE OF CONTENTS

LIST OF FIGURES

LIST OF TABLES

LIST OF SYMBOLS

D_A	Angular diameter distance
g_{ff}	Gaunt corrections for quantum mechanical effects
k_B	Boltzmann constant
L_{cool}	Total cooling rate
$M_\odot$	Solar Mass
$\dot{M}_{cool}$	Cooling flow
m_e	Electron mass
M_{gas}	Gas mass of cluster
n_e	Electron density
n_H	Hydrogen column density
r_{cool}	The cooling radius
t_{cool}	Cooling time
T_{gas}	Gas temperature
t_{Hubble}	Hubble time
z	Redshift
$Z_\odot$	Solar Metallicity
ϵ_ν	X-ray emissivity
ϵ_v^{ff}	Total emitted free-free power
ΔE	Excitation energy
$\sigma(E)$	Photoelectric cross-section
Ω	Collisional strength

LIST OF ACRONYMS/ABBREVIATIONS

AGN	Active Galactic Nuclei
APEC	Astrophysical Plasma Emission Code
CALDB	Calibration Database
CCD	Charge-Coupled Device
DEC	Declination
d.o.f.	Degrees of Freedom
EPIC	European Photon Imaging Camera
ESA	European Space Agency
FOV	Field of View
HEASOFT	High Energy Astrophysics Software
ICM	Intracluster Medium
LHB	Local Hot Bubble
MOS	One of the two EPIC Cameras
obs	Observation
PHABS	Photoelectric Absorption Model
pn	One of the two EPIC Cameras
RA	Right Ascension
SN	Supernova
SNIa	Supernova Type Ia
SNcc	Supernova Core Collapse
SNIb	Supernova Type Ib
SNIc	Supernova Type Ic
SNII	Supernova Type II
XMM	X-ray Multi-Mirror Mission
XSPEC	X-Ray Spectral Fitting Package

1. INTRODUCTION

Galaxy clusters are the largest gravitationally bound objects in the universe with a radius of ∼2 Mpc. A typical cluster contain 10's to 100's bright galaxies and also 1000's of fainter galaxies [1]. These galaxies, however, consists only ∼3% of the total mass that is approximately $10^{14}M_{\odot}$ to $10^{15}M_{\odot}$. In fact, the visible baryonic matter is only ∼15% of the total mass and the other ∼85% is dark matter [2, 3]. The fact that dark matter dominates galaxy clusters indicates that the predominant mass in Universe is dark matter [4].

What about the remaining ∼12% percent of the total mass which is ∼4 times of the galaxies and stars? It is the hot intracluster medium which galaxies and stars are embedded in. The density of this hot gas is between $\sim 10^{-2}cm^{-3}$ and $\sim 10^{-2}cm^{-3}$, which is so tenuous that it is only ∼1% of the interstellar gas in a galaxy [5]. Despite being tenuous, intracluster medium (ICM from now on) reaches temperatures of $10^7 - 10^8$ K [6]. This gas is created around a redshift of $z \sim 2- \sim 3$ at which star formation is peaked. In this era early Population III stars had ejected metals into the surrounding medium which helped the gas cool down enough to form stars [7]. Population III stars are defined to express stars which are composed entirely of hydrogen and hellium (and very little traces of lithium and beryllium). This composition is due to the fact that they are formed from the material left over from the Big Bang. These stars produced metals by nucleosynthesis and ejected them to their surroundings by supernova explosions and therefore formed the ICM.

The massive gravitational well of clusters heats the ICM up to tens of millions of degrees [8] and therefore the hot plasma emits photons. Because of its great temperature, photons are emitted in the soft X-rays and can only be detected by the X-ray telescopes. Among the plasmas that we are able to study, the ICM is the hottest. Merging clusters, on the other hand, release so much energy that it is the largest energy after the Big Bang itself. It can be hot up to two orders of magnitude larger than the temperature of the core of Sun. Galaxy clusters also create the best gravitational lensing effects because its great gravitational potential enhances the effect of light deflection. These characteristics of the ICM make galaxy clusters the most worthwhile study objects for X-ray imaging. Another reason why galaxy clusters provide informative X-ray spectra is their tenuous density. Its tenuous form makes it in collisional ionization equilibrium and provides better interpretation of the X-ray spectra comparing to denser objects such as stars.

In this thesis, the general outlines of the clusters of galaxies are explained with a brief historical background. Then, general enrichment mechanisms are briefly explained, which is followed by the brief investigation of XMM-Newton observatory.

Our main research interest is the Toothbrush cluster of galaxies.
1RXS J0603.3+4214 is a merging cluster at z=0.225 in which a radio halo and three radio relics appear [9]. One of the radio relics gives the name Toothbrush because of the shape of it. Although there have been previous studies on the Toothbrush, temperature and abundance profile have not been generated. By studying how the shock affected these parameters, we will be able to say more about merging galaxy clusters and specifically about Toothbrush cluster here and it will be its first study in the published literature so far.

1.1. Overview of Galaxy Clusters

In this section, we explain the historical background of galaxy clusters, and then we investigate the basic properties of it.

1.1.1. History of Galaxy Clusters

Historical background of galaxy clusters goes back to 18th century. In order to discover the history of cluster of galaxies, we took Andrea Biviano's paper "From Messier to Abell: 200 Years of Science with Galaxy Clusters" as our guide.

The studies of cluster of galaxies go back to as early as 1784 [10]. French astronomer Charles Messier listed 103 nebulae in his "Catalogue des n´ebuleuse et des amas d'´etoiles que l'on d´ecouvre parmi les ´etoiles fixes, sur l'horizon de Paris". Nebula is a cloud of dust and ionised gas of hydrogen, helium and other gases in the interstellar medium. 30 of the nebulae in C. Messier's catalogue are now identified as galaxies. Messier, however, was not particularly interested in nebulae. His main research was on comets and he needed to identify the positions of nebulae in order not to misidentify them with comets.

William Herschel and his sister Caroline Herschel were also the pioneers of the field. William was a musician who took interest in physics long after he pursuits his music career. After reading a popular astronomy book, he has become a good telescope crafter and took his sister with her to help his researches. Caroline and William, then became the famous discoverers of comets and classifier more than 2500 nebulae. In 1785 "On the Construction of the Heavens[11]" was published where W. Herschel suggested that the "sideral system we inhabit" is a nebula. He also described the Coma cluster of galaxies as, "that remarkable collection of many hundreds if nebulae which are to be seen in what I have called the nebulous startum of Coma Berenices".

In the same paper, her sister Caroline Herschel discovered M 31, NGC 205. In fact, with M 32 these three galaxies make a triplet of galaxies similar to the triplet of Milky Way and two Magellanic clouds. Another object, M 33 was listed in Messier's catalogue. This means 7 members of the Local Group of galaxies were already discovered by that time (Local Group is the galaxy cluster that includes the Milk Way, having diameter of 3 Mpc and mass of $2 \times 10^{12} M_{\odot}$)! In 1864, William Herschel's son John F.W. Herschel completed his General Catalogue of Nebulae and Cluster of Stars covering more than 6000 nebulae. He has hinted the existence of the Local Supercluster back then, considering Virgo concentration he said "being regarded as the main body of this system" and Milky Way "placed somewhat beyond the borders of its densest portion, yet involved among its outlying members"[12]. A supercluster is a group of galaxy clusters and groups bound together gravitationally. The Milky Way for example, is located in the Local Group galaxy group which is in the Virgo Cluster and the

Virgo Cluster is a part of Laniakea Supercluster. Other memorable names of the same era that needed to be mention are d'Arrest[13] and Prector[14] identifying new charts of nebulae in the Virgo and Coma clusters, and also Dryer[15] and Stephan[16]. As time went on and with the help of advanced technology, new methods of discovery have arised. With photographic methods, 300 nebulae were discovered in the Coma cluster by 1918. In 20th century, the main discussion was whether or not discovered nebulae were external to our galaxy or not. There even organised "The Great Debate (1920)" on the subject, resulting no any clear winner.

It was discovered in 1904[17] that there is an asymmetry in the scattering of the nebulae with respect to the galactic plane. Most of the discovered nebulae were located in the Northern Hemisphere. In 1923, Reynolds[18] made a remark on the asymmetry, "many of the spirals 10' diameter and upwards lie along 100 degree, and form part of a well-marked band of nebulae passing over the north galactic pole, which comes out conspicuously if the spirals ranging down to 2' diameter are plotted together." which suggest a binding among the nebulae, a direct clue to Local Supercluster.

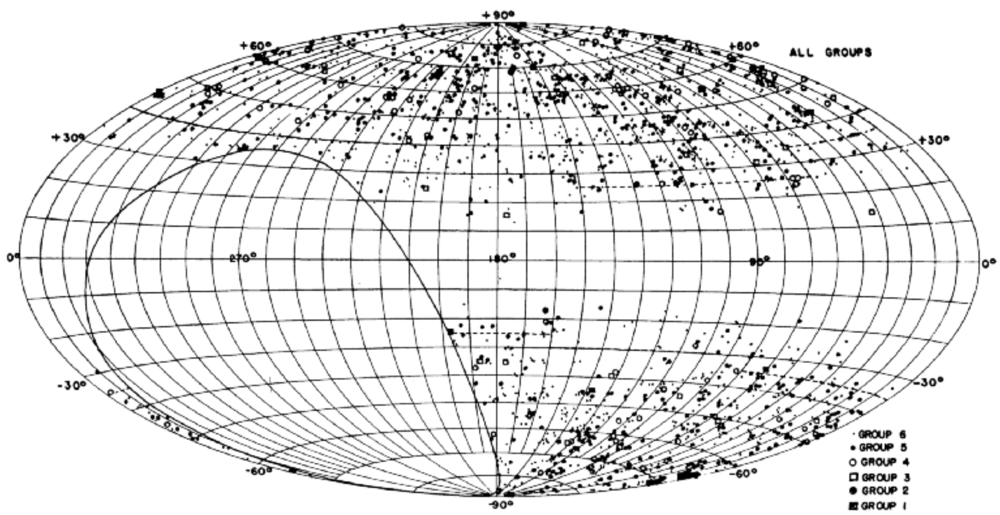

Figure 1.1. Distribution of clusters of galaxies ASD[19]. "The distribution in galactic coordinates of the catalogued clusters in richness groups 1-5 and distance groups 1-6, inclusive. The plot is on an Aitoff equal-area projection."

E. Hubble, on the contrary, protested the argument. In 1936 he suggested that the distribution is moderately uniform and added that "no organization on a scale larger than the great clusters was known. Nevertheless, he is the one who gave the name "Local Group" to our galaxy cluster which he recognized Milky Way as a member of it. By the time of Hubble, the number of discovered nebulae was rised to 60 millions.

Hubble's view of a uniform distribution of galaxies was dismissed after the Second World War. In 1956 M. Humason, N. Mayall and A. Sandage conducted a twenty years of spectroscopic observations of more than 800 redshift of galaxies (75 in Virgo and 23 in Coma). They stated their findings as "increasing evidence" for a general clustering in the universe. The discussion on local cluster was done, however astronomers now would debate about the idea of superclusters. "The Local Supergalaxy" phenomenon was increasingly accepted among astronomers. F. Zwicky, however, was still denying the existence of superclusters. His point of view, on the other hand, was different from E. Hubble's. He did not deny that there is no organization on a scale that large, he considered galaxy clusters to be much larger than recognized, almost sizes of superclusters. G. O. Abell stated that[20] his opposition was purely semantic. At the end, F. Zwicky himself discovered a supercluster[21] but he refused to call it a supercluster. He instisted that clusters "fill the universe just as the bubbles fill a volume of suds", refering his idea that the non-uniform distribution of clusters was only due to the obscuration effects of inter-galactic dust.

Meanwhile, the discovery techniques have been improving. W. A. Baum[22] pointed that clusters at redshifts ~ 0.5 might be most easily detected by moving redwards the observing waveband. R. Minkowski[23] proposed that collisions between galaxies could create radio emission due to the dense environment, he speculated that clusters could be found easier around radio-galaxies.

The searching itself has become more systematic rather than serendipitous discoveries of 18th century. A catalogue of galaxies and cluster of galaxies is published in 1975[24] and almost 10000 clusters were identified.

One year later, G. O. Abell published his milestone paper called “The distribution of rich clusters of galaxies”. G. O. Abell did not try to construct a wholesome catalogue, he focused on only rich clusters; which made him first to show the distribution of cluster richness. He stated, “during the course of the plate inspections, many thousands of clusters and groups of galaxies were recognized which were not catalogued because they obviously were not sufficiently rich to insure their essentially complete identification.”. His paper has become so important and famous that rich clusters are now called as Abell clusters. Still, most people base their analysis on G. O. Abell’s catalogue. At last astronomers had the opportunity to study clusters as a group of objects rather than single individuals with the publications of catalogues.

About the supercluster discussion; in his mentioned paper G. O. Abell showed that “clusters of clusters” exist by his magnitude-based cluster distance estimations to establish the fact that average size of superclusters is ~ 60 Mpc. G. de Vaucouleurs[25] also suggested that 85% of all nearby galaxies belong to groups and superclusters could well overlap and fill the available space.

Another major milestone in the subject was the drawing[26] the 3-dimensional structures of Coma, which can be seen in Figure 1.2., Hercules, Hydra-Centaurus, Perseus and Pisces superclusters. On the drawn picture of Coma, G. O. Abell said[27]:

“The picture that suggests itself is that of a large inhomogeneity or region of space containing galaxies, groups, and clusters, in which what is commonly called the Coma cluster is simply a dense concentration, rather like an urban center in a large metropolitan area.”.

It was now believed that galaxies form clusters and clusters form superclusters. F. Zwicky, however, was still denying that any supercluster formation. But nonetheless evidences against F. Zwicky had been revealing. In 1978, M. Joeveer and J. Einasto[28] showed that clusters of galaxies together form chains in the vast space of the Universe, the main structure of the Universe was even compared to cells[29], with galaxy clusters concentrated towards the walls of cells.

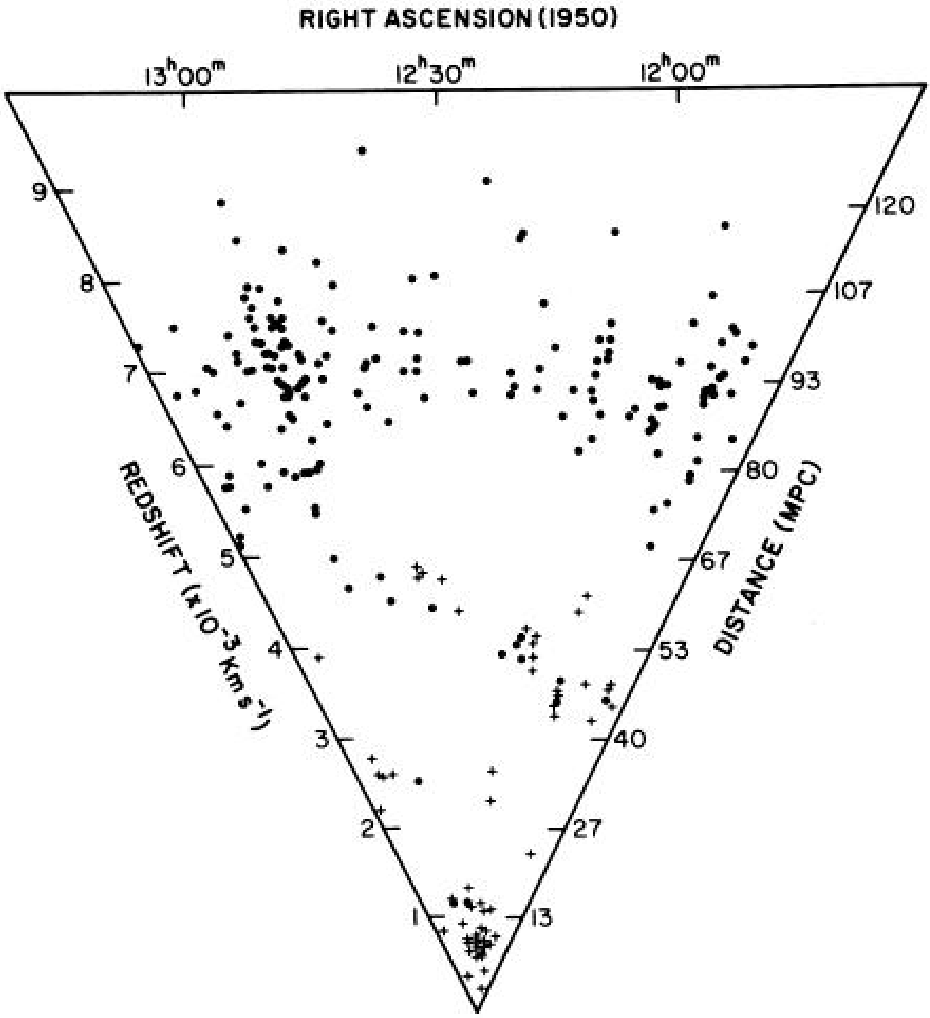

Figure 1.2. The wedge diagram of the Coma supercluster from [26]"

Cluster connecting filaments and voids were also identified[26]. Galaxy filaments are thread-like structures with a length of 50 to 80 megaparsecs containing superclusters. Voids, on the other hand, are the relatively empty area containing very few or no galaxies with a diameter of 10 to 100 megaparsecs.

Astronomers continue to use clusters as tracers of the Large Scale Structure of the Universe. G. O. Abell[30] revised his proposition in 1983, saying that superclusters are interconnected because their separations are comparable to their sizes.

In the late 1980s, structures larger than superclusters began to be discovered. In 1987, R. B. Tully discovered Pisces–Cetus Supercluster Complex. These so called “cluster of superclusters” are now defined as galaxy filaments.

1.1.2. Basic Properties of Galaxy Clusters

The hot gas in the galaxy cluster cores has a cooling time t_{cool} [31],

$$t_{cool} = \frac{\gamma}{\gamma - 1} \frac{nkT}{n^2 \Lambda(T)} \sim 10^8 - 10^9 yr \tag{1.1}$$

in which n is the density of the ICM and T is the temperature of it. $\Lambda(T)$ is the radiative cooling function and γ is the adiabatic index. It can be seen that $t_{cool} \propto 1/n$. This means that denser the medium is, cooler it is in a given time, since t_{cool} is shorter for dense parts. In the cores of galaxy clusters ICM is the denser, so it is clear that cores are cooler! Cluster of galaxies with that property are called $cool - core$, which is the most common for relaxed clusters. The cooling radius r_{cool} is where $t_{cool} \sim t_{Hubble}$. The gas inside r_{cool} cools and flows towards the center if there are no external energy source. This flow is called as ”cooling flow”[32],

$$\dot{M}_{cool} = \frac{L_{cool}}{\frac{\gamma}{\gamma - 1} kT} \mu m_p \sim 10^2 - 10^3 M_{\odot} yr^{-1} \tag{1.2}$$

where L_{cool} is the total cooling rate inside r_{cool} and μ is the mean particle atomic weight. In reality, however, the flow is not exactly like that. Observations [33] show that the actual rate of gas cooling to low temperature is below $\sim 10\%$! This suggest that there must be a source of heat that halts the cooling. Notice that if the cooling is prevented, star formation from the gas is also be interrupted.

In 1990s, it became clear that there is a supermassive black hole located at the center of the dominant cluster galaxy could be the missing source of heat. This region is called Active Galactic Nucleus (AGN).

Rich cluster of galaxies inhabits massive elliptical galaxies at their cores, and the elliptical galaxies host black holes with masses larger than $10^9 M_\odot$. The accretion of them releases 10^{47} $ergs^{-1}$ that is much more than the needed heating energy of the cooling gas.

1.1.3. Merging Clusters

Galaxy clusters are the largest bounded objects in the universe, and they grow by merging with other clusters [34]. Cluster merging creates great amount of energy, approximately 10^{63} to 10^{64} ergs [35]. This energy creates disturbance in the intracluster medium and makes it emit X-rays and by investigating X-ray emissions, we can tell that most of the clusters are in merging process. The merging caused disturbance occasionally creates travelling shock waves with Mach numbers below 4 [36]. Mach number represents the ratio of flow velocity to the speed of sound in the local medium.

In some cases, merging clusters emit radio emission. These radio relics and halos are independent from the particular galaxies inside the cluster, they are originated from ICM that is disturbed by the merging [37, 38] These extended radio emissions have two forms, radio relics that mostly located at peripheries of the cluster and radio halos that are in the central regions of the cluster [36, 39]. Morphologically, halos are smoother and have circular shape while relics are arc-like.

Radio halos are generally have a size of one Mpc and they are unpolarized. We have two models that explain their origin. (1) Cluster mergers creates turbulence in the ICM and generated turbulence re-accelerate relativistic electrons [36]. (2) The turbulence leads to proton-proton collisions and electrons are by-products. Radio relics, on the other hand have three different types. (1) Radio relics that are found in the peripheries of the cluster where particles are accelerated by shock waves [38]. (2) Active galactic nucleus relics are another class of radio relics which gathers old plasma near AGN. (3) Radio phoenices are AGN relics that is affected by a shock wave.

1.2. Enrichment of Intracluster Medium

We have stated that ICM is a hot gas with enriched structure. But how those metals happen to exist in such environments that intuitively thought to be deserted? In order to answer this question we first need to establish how those metals originate in the first place.

In 1920s, it was first proposed [40, 41] that stars may be using hydrogen and other light elements as their source of energy by nuclear fusion. This suggests that heavier elements are formed in the stars. Similarly, in 1939 [42] basic features of stellar nucleosynthesis are defined as followings, i) The proton-proton chain reaction in low mass stars ($< 2.2M_{\odot}$) creates helium nucleus in the star as two proton form a helium atom (PP-I branch in Equation 1.3).

$$\begin{aligned}
{}^{1}\mathrm{H} + {}^{1}\mathrm{H} &\longrightarrow {}^{2}\mathrm{H} + \mathrm{e}^{+} + \nu + 0.42\mathrm{MeV} \\
{}^{2}\mathrm{H} + {}^{1}\mathrm{H} &\longrightarrow {}^{3}\mathrm{He} + \gamma + 5.49\mathrm{MeV} \\
{}^{3}\mathrm{He} + {}^{3}\mathrm{He} &\longrightarrow {}^{4}\mathrm{He} + {}^{1}\mathrm{H} + {}^{1}\mathrm{H} + 12.86\mathrm{MeV}
\end{aligned} \tag{1.3}$$

ii) The CNO Cylce (shown briefly in Equation 1.4) in which helium is formed with the catalysts of carbon, nitrogen and oxygen.

$$4\,{}^{1}_{1}\mathrm{H}{+}2\,\mathrm{e}^{-} \longrightarrow {}^{4}_{2}\mathrm{He}{+}2\,\mathrm{e}^{+}{+}2\,\mathrm{e}^{-}{+}2\,\mathrm{v_e}{+}3\,\gamma 24.7\mathrm{MeV} \longrightarrow {}^{4}_{2}\mathrm{He}{+}2\,\mathrm{v_e}{+}3\,\gamma 26.7\mathrm{Mev} \tag{1.4}$$

Although the steps proposed are true, they do not fully explain the origin of metals as the proposal is insufficient to tell how the heavier elements can come into existence. It was speculated [43] that the heavy elements had originated at the first moments of the Universe. Later, it is proposed that the heavy elements or "metals" are created in the core of a collapsing star. In 1952, absorption lines of technetium (Z = 43) are detected [44] in the R Andromeda and similar red variable stars' spectra. This finding may suggest that heavy elements are not forged at some time in the past, it is still ongoing. The forming of heavier metals are explained in Section 1.2.3. but for now let us focus how the elements up to Fe are produced in the stars.

1.2.1. How Does Stellar Nucleosynthesis Work?

As explained, main source of energy of the stars is the nuclear fusion. The most basic method is to transform hydrogen into helium while creating great amount of energy so that it prevents stars to collapse by gravity. Stars with greater masses die faster, forming a wider range of metals comparing the lower mass ones.

Low mass stars are able to perform hydrogen fusion while medium mass stars are able to conduct helium fusion[45]. High mass stars, on the other hand, make further steps of nuclear fusion possible so that metals up to Fe are formed.

The long-living low mass stars slowly form helium from hydrogen that results in accumulating helium in their cores. They cannot ignite any formation beyond that. In medium-mass stars, however, the gravitational potential that helium core creates piles up hydrogen in a shell that surrounds the core. The gravitational potential creates great pressure to the shell heating the hydrogen much enough to form helium rapidly via nucleosynthesis, causing the star to expand[45]. Next, the so called burning hydrogen shell heats the helium core up to the sufficient energy that carbon begins to from as helium undergoes the fusion synthesis. At this stage the star has become a red giant at its brightest state.

Evolution of the medium mass stars end here, but if the star is a high mass one, this ”forming and heating” process can continue up to the elements of H, He, C, Ni, O, Si and Fe respectively (there also exist traces of Mg and Ne) creating an ”onion” structure (Figure 1.3.). When Ni forms Fe, the reaction consumes energy rather than generating since nuclear fusion is energetically inefficient for higher isotopes.

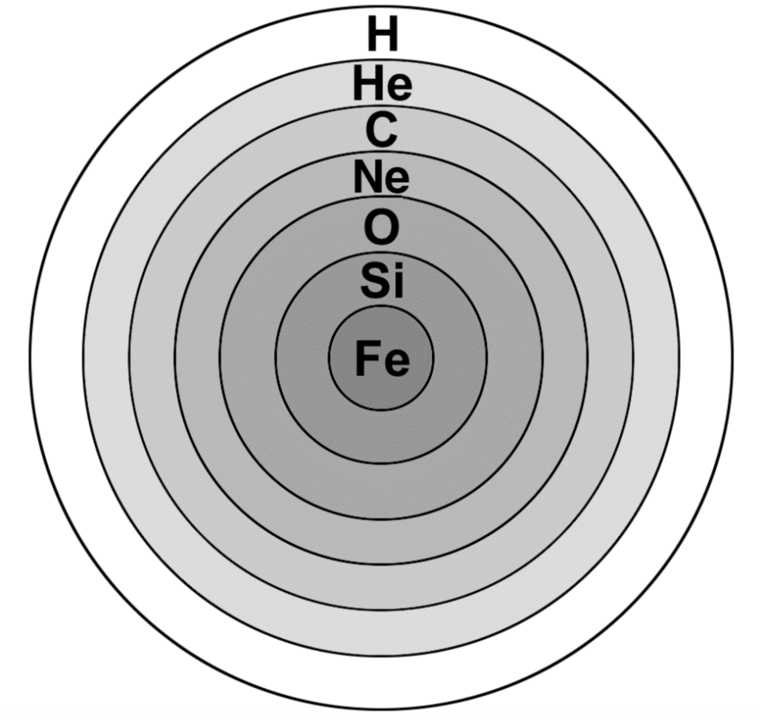

Figure 1.3. A diagram illustrating the “onion” structure of a star. Credit:NASA

As a result, accumulated Fe has ingested the energy and also creates a great gravitational potential that increases the core density up to electron degeneracy. Electron degeneracy occurs at densities $\sim 10^6 kg/m^3$. Electron degeneracy pressure is a term which comes from the Pauli exclusion principle that forbids to identical half-integer spin particles (electrons in this case) from occupying the same quantum state simultaneously. Electron degeneracy pressure opposes the compression of matter into smaller volumes. This density leads to the first type of enrichment mechanism of ICM.

1.2.2. Core-collapse Supernovae (SNcc)

When the core density of a massive star reached the Chandrasekhar limit ($1.4M_{\odot}$) the electron degeneracy pressure cannot hold the gravitational contraction. Protons start to capture electrons leading the creation of neutrons and neutrinos. The contraction halts when the core reached to neutron degeneracy pressure. The immediate stop of contraction generates powerful reverse shock to the upper layers travelling about

25% to 50% speed of light. The shock heats the upper layers of material leading to synthesis of more elements namely O, Ne and Mg. Although O, Ne and Mg are produced inside the stars before the supernova, they are consumed in the process. Almost all the O, Ne and Mg in the Universe and half of the portion of Si and S produced by Core-collapse supernovae (Type SNcc) [46]. Heavier elements like Ca, Ar, Fe and Ni are sometimes synthesized but at much lower quantities.

SNcc are linked to Type II supernovae (supernovae that has hydrogen in their spectrum) and Type Ib (supernovae that lost its hydrogen layer) and also Type Ic (supernovae that lost its hydrogen and helium layers).

1.2.3. Type Ia Supernovae

We have stated that when a medium mass star ($< 8M_{\odot}$) stop fusion reaction when it reaches to carbon. This results in a carbon-oxygen core and dissipated matter as a nova. The remaining carbon-oxygen core is called a White Dwarf and it is the main cause of Type Ia supernovae. White dwarfs catches companion stars and other objects because of their gravitational potential, as progenitor theories suggest[47]. When the white dwarf accrets material from its companion object, it gets heated as carbon undergoes explosive burning which results in re-ignition. Thermonuclear fusion makes the white dwarfs unstable as it cannot expand and cool down. Although the exact mechanism is still unknown, the object is entirely disturbed and a violent explosion eject its material to the interstellar medium.

Notice that unlike SNcc, SNIa is not a result of death of a massive star. Furthermore, there are no remaining stellar object while in SNcc the core collapses to form a remaining neutron star or a black hole.

Most of the Ar, Ca, Cr, Mn, Fe and Ni and about half of the Si and S in the Universe are formed by SNIa supernovae. Similar to the mechanism in SNcc; C, O, Ne and Mg are the fuels of this process and do not remain considerably after the explosion.

Figure 1.4. Artist impression of one of the Type Ia supernova theories. Credit: NASA

In order to estimate the expansion of the Universe SNIa are used as standard candles to measure cosmological distances[48].

In sum, C, N and traces of Ne and Mg are synthesized in the asymptotic giant branch stars. Almost all of the O, Ne, Mg and nearly a half of the Si and S in the Universe are formed in SNcc supernovae. Type Ia supernovae, on the other hand, forms the major part of Ar, Ca, Cr, Mn, Fe, Ni [49] and about one half of the Si and S in the universe. Even heavier elements than what we have discussed are forged in extravagant events such as neutron star mergers [50] and compact stellar binary assembly [51]

The produced metals go beyond the host galaxy and reach ICM because of the supernova explosions. Secondary factors like ram pressure also cause the ICM enrichment, galaxies lose their metals to the ICM as they travel inside the medium.

1.2.4. Abundance Measurements of ICM

The spectral lines of all elements between carbon and zinc lie between the soft X-ray band of 0.1 and 10 keV. So studying this interval of X-ray band is suitable for abundance studies in cluster of galaxies. The hot ICM is almost in collisional ionisation equilibrium so detecting emitted X-ray spectrum is rather easy[52]. In 1996 ASCA became the first satellite[53] to make it possible to measure the abundances of

O, Ne, Mg, Si, S, Ar, Ca, Fe and Ni. From the studies of ASCA, it is revealed that ICM was enriched at the early period of formation by core-collapse supernova products. Type SNIa joined the enrichment later[53].

Deep abundance studies in larger samples of clusters became available after the launch of XMM-Newton which is explained in Secton 1.4. Expected type SNIa models were tested [54] as profiling the core regions and improved models by adding new constraints. It is shown that[54] the calcium abundance turns out to be systematically higher than models (Figure 1.5.). Best possible explanation to this problem is that the main mechanism in SNIa are the progenitor systems in which helium is accreted on the white dwarfs. The reason of required helium is that its fusion expected to create more calcium.

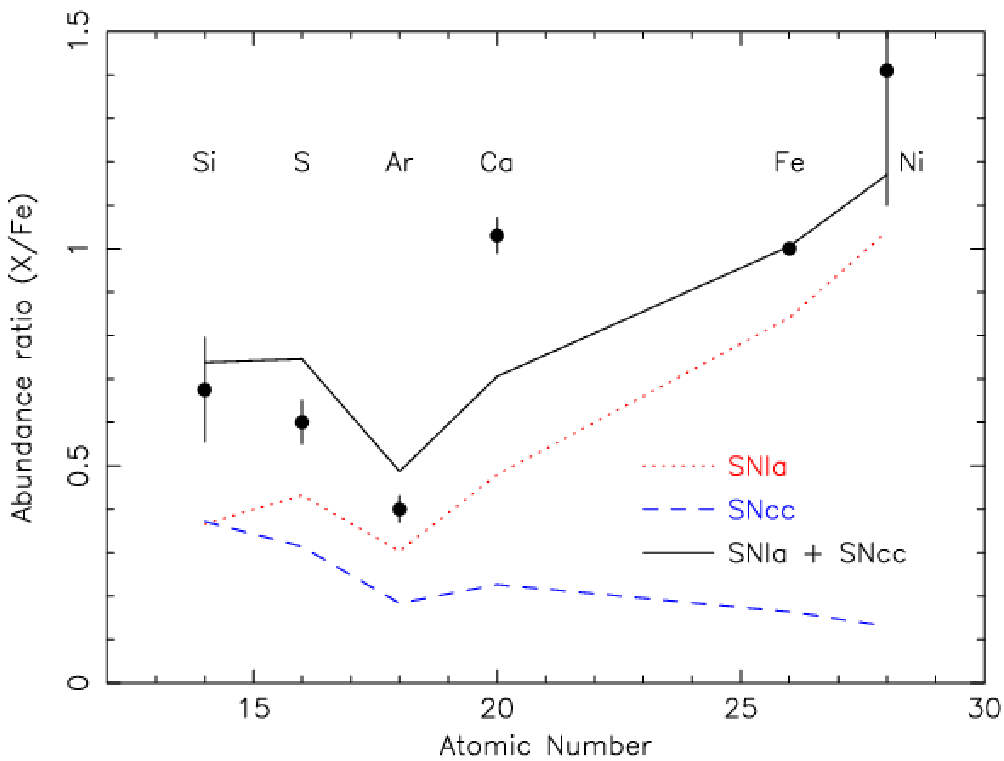

Figure 1.5. Abundance ratios fitted with WDD2 SNIa model [49] and SNcc model with an initial metallicity Z = 0.02. The calcium abundance seems to be underestimated. Credit: [54]

The relative contribituions of SNIa and SNcc can be found by their ratio if a combination of SNIa and SNcc model fits. In 2012, Bulbul[55] developed an APEC model (APEC model is used in this thesis and is explained briefly in Section 3.3.1.) extension that end up deriving a 30-40

What about enrichment sources apart from supernova explosions? XMM-Newton is able to measure carbon and nitrogen abundances. It is found [8] that elliptical galaxies are highly abundant of carbon and nitrogen. Nitrogen, however, cannot be produced considerably by supernovae, they are formed by metal-poor massive stars or asymptotic giant branch (AGB) stars. Therefore the high nitrogen abundance in ICM is very possible originated in a population of intermediate-mass AGB stars [5].

Another surprising finding is the distribution of iron abundance in the outskirts of clusters. A recent detailed study [8] showed that at the outskirts of the Perseus cluster the iron abundance is surprisingly distributed smoothly. The explanation to that is the early enrichment scenario even before $z \sim 2$. The very important result originated from this study is that chemical enrichment occurred very early, probably before the formation of clusters.

In 2012[56] abundances of a sample of high redshift clusters between z = 0.3 – 1.3 was studied. This study shows that there is no significant trend in metal abundance even though the scatter in the measured metal abundance as a function of redshift is large. This suggests that the chemical enrichment mechanisms have not contributed significantly to the enrichment since z = 1.3

1.3. Emission Mechanisms in Galaxy Clusters

Analysis of the cluster of galaxies mainly depends on the modelling of X-ray spectra. In the following sections, emission mechanisms are explained while the models to calculate the radiation from the ICM in thermal equilibrium are explained in Section 3.3.1.

1.3.1. Continuum X-ray Emission

The main emission mechanism of hot ICM plasma (and therefore of clusters) is thermal Bremmstrahlung (31). There are also small contributions of radiative recombination and two photon emission process, however since they are minor ones and Bremmstrahlung is the dominant mechanism that shapes the X-ray, we only focus on Bremmstrahlung. Bremsstrahlung is an electromagnetic radiation that is caused by the deceleration of charged particle when deflected by another charged particle. In order to maintain the law of conservation of energy, kinetic energy that the moving particle loses is turned into radiation. The Bremsstralung emitted from hot ICM gas is called free-free radiation since the radiation is emitted by free charged particles, not part of an atom or molecule. The total emission of ICM population is called thermal bremsstrahlung. The hot diffuse ICM gas is assumed to be at a uniform temperature and are distributed according to the Maxwell-Boltzman velocity distribution,

$$f_e(v) \propto exp(\frac{-m_e v^2}{2k_B T_{gas}})v^2 dv \tag{1.5}$$

where m_e is the electron mass, k_B is the Boltzmann constant and T_{gas} is the temperature of the plasma.

Hot gasses that are about $10^7 K$ emit Bremsstrahlung X-rays. We have explained that ICM is an optically thin medium. This is very fortunate, in optically thin mediums the gas is not able to absorb its own radiation considerably so the spectrum of observed X-rays is the same as the produced spectrum.

Total emitted free-free power ϵ_v^{ff} in the cloud per unit volume (the emissivity) of an ion of charge Z at a frequency ν in a plasma with an electron temperature T_g is given by[57],

$$\epsilon_v^{ff} = \frac{2^5 \pi e^6}{3m_e c^3}(\frac{2\pi}{3m_e k})^{1/2} Z^2 n_e n_i g_{ff}(Z, T_g, v) T_g^{-1/2} exp(-\frac{h\nu}{kT_g}) \tag{1.6}$$

where n_i and n_e are the number densities of ions and electrons respectively, $g_{ff}(Z, T_g, \nu)$ is the Gaunt corrections for quantum mechanical effects[58]. It is clear that the main emission dependants are the temperature of plasma and the density of the ions. Considering ICM is optically thin plasma, n_{ei} sum over frequency gives us the total emmisivity,

$$e \sim n_e^2 T_g as^{1/2} \tag{1.7}$$

1.3.2. Line X-ray Emission

Line emission is the another dominant X-ray radiation source. By looking at the line emissions, we can detect the abundance of metals since each metal emits a specific spectra (Figure 1.6.). Line emission originates from the electron transition between two different energy states. The line emmisivity due to a collisionally excited plasma is given by[59],

$$\int e_\nu^{line} d\nu \propto n_i n_e \frac{\Omega(T_{gas})B}{w_{gs,i}} T^{-1/2} \nu.exp(\frac{-\Delta E}{k_B T_{gas}}) \tag{1.8}$$

where B is the branching ratio meaning the probability of decay into a lower state, Ω is the collisional strength, $h\nu$ is the energy of the transition and ΔE is the excitation energy above the ground state of the excited level.

1.4. XMM-Newton Satellite

There has been many X-ray satellites launched for different purposes. There are three missions to be mentioned that are still in use. *Chandra* (launched in 1999) has exceptional spatial resolution and it is perfect to study substructures in ICM. *Suzaku* (launched in 1999) on the other hand, has poorer resolution which is an advantage

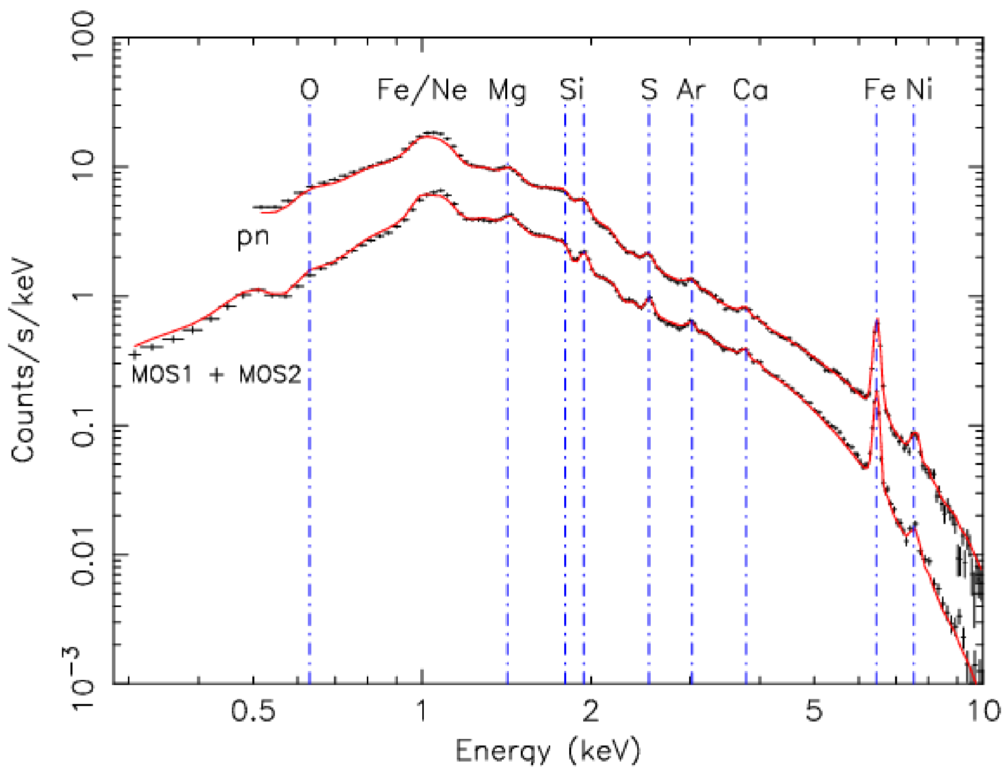

Figure 1.6. EPIC spectrum of the cluster 2A 0335+096 with an exposure time of 130 ks. The metal emission lines are specified with blue dots. Credit:[8]

to study outskirts of clusters because of its low instrumental background. Finally, $XMM - Newton$ (launched in 1999) has largest effective area providing better spectral resolution is better for studying abundances in the clusters. For creating abundance and temperature distribution in the Toothbrush cluster of galaxies, we decided to study $XMM - Newton$ observations.

XMM-Newton observatory also known as X-ray Multi-Mirror Mission was launched in December 1999 by European Space Agency (ESA) as one of the cornerstones of ESA Horizon 2000 programme. The largest scientific satellite ever launched by ESA is XMM-Newton[60] and it is 4 tonne and 10 m long. The orbit of the observatory has a ∼48 hour period, which is remarkably eccentric. The perigee is 7,000 km and apogee of 114,000 km and the inclination is approximately $-40°$. This highly eccentric orbit helps the main cameras to cool down to the degrees $-80°$ to $-100°$ only with the

Figure 1.7. Artist's impression of the XMM-Newton spacecraft in orbit around the Earth. Credit: NASA

help of passive radiators. The satellite consists of four main parts [60] and from top to bottom they are summarized in details.

- At the very front of the satellite there is the Focal Plane Assembly (FPA). It includes the Focal Plane Platform (FPP) that consists of focal-plane cameras. First, two Reflection Grating Spectrometer (RGS) and two MOS and one pn European Photon Imaging Camera (EPIC) cameras, which are explained in detail in Section 1.5.2. In order to cool the detectors down, cooling radiators surround the cameras.
- The 6.80 m long Telescope Tube is made of carbon fibre and placed between FPA and Mirror Support Platform (MSP). It has upper and lower modules.
- The Mirror Support Platform (MSP) carries three mirrors assemblies, the Optical Monitor and two star trackers.
- The Service Module (SVM) contains the satellite subsystems supplying required resources to the observatory. The Telescope Sun Shield (TSS), two S-band antennas and solar-array wings are also mounted on SVM

Figure 1.8. Focal Plane Assembly Credit: NASA

Figure 1.9. The Telescope Tube Credit: NASA

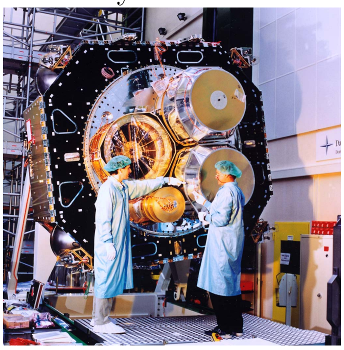

Figure 1.10. The Mirror Support Platform Credit: NASA

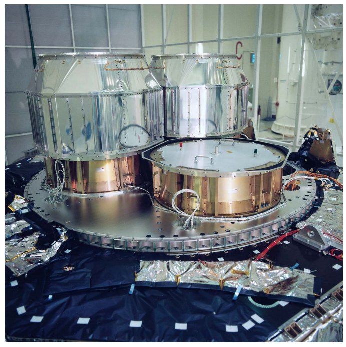

Figure 1.11. The Service Module Credit: NASA

1.4.1. Telescopes

The unique feature of XMM-Newton is its remarkable effective area. It owes this quality to the design of its three telescopes. The focal length of the telescopes is 7.5 meters and the diameter of the largest mirror is 70 cm. XMM-Newton telescopes are sensitive to the low energies which is 2 keV and they do not abandon the area at high energies which is 7 keV. The telescopes consist of 58 Wolter I grazing-incidence mirrors and they employ 30' shallow grazing angle so that they provide decent reflectivity at high energies.

XMM-Newton mirrors are best suitable in the energy range from 0.1 to 10 keV, with most efficiency around 1.5 keV. Every telescope has collecting area of 1900 cm^2 for energies up to 150 eV, 1500 cm^2 at 2 keV, 900 cm^2 at 7 keV, and 350 cm^2 at 10 keV.

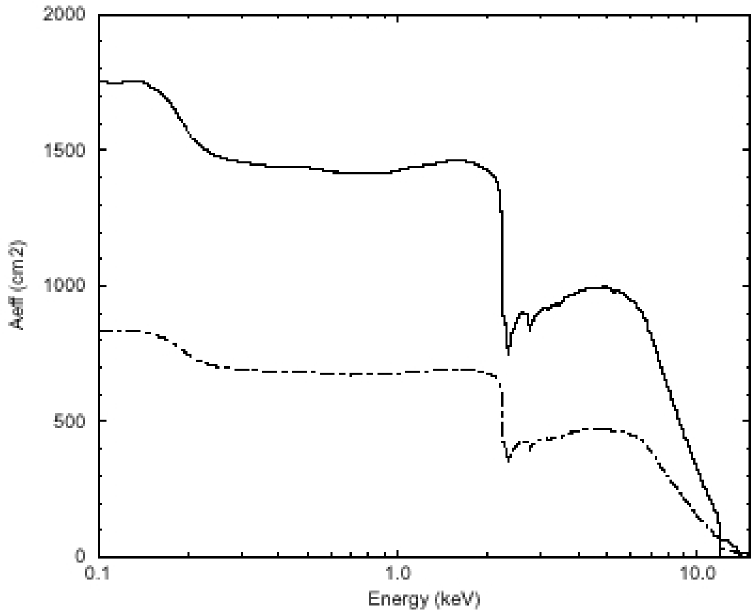

Figure 1.12. Effective area of the XMM-Newton telescopes. Solid line is without Reflection Grating Assembly (RGA) and dot-dashed line is with RGA. Credit:[61]

Each telescopes has 58 mirrors which were produced from superpolished gold coated mandrels applying a nickel electroforming technique[62]. 16 spokes of a single spider joins mirrors together on their entrance aperture.

Low energy electrons reflected by the mirrors can reach the focal plane detectors. In order to prevent this an electron deflector is placed in the exit aperture. This deflector creates a circumferential magnetic field and stops the reflected low energy electrons arrive to the detectors.

1.4.2. Basic Properties of EPIC

XMM-Newton satellite has three X-ray CCD cameras, comprising the European Photon Imaging Camera (EPIC). A CCD consists of coupled capacitors. When an incident photon hits to the semiconductor layer of the CCD, the incoming photon generates an electron cloud. The energy of this cloud of electrons is proportional to the incoming photon. Between the gates of CCDs potential wells are created and the generated electrons are stored in pixels.

EPIC has three cameras, one pn and two MOS. MOS cameras have a better spatial resolution while pn has a better time resolution. They both execute remarkably sensitive imaging observations over the field of view (FOV) of the telescope. They have 30 arcmin FOV within the energy range from 0.15 keV to 15 keV.

MOS has seven EEV type 22 front-illuminated CCDs in its cameras [60]. At the focal point on the optical axis, there is the central CCD. In order to make the focus for off- axis sources better, the other six are 4.5 mm away from the mirror. The imaging area of each CCDs is approximately 2.5 x 2.5 cm which makes in total 62 mm in diameter (28.4 arcmin) since there are seven of them. On the Field of View (FOV) one pixel is equivalent of 1.1 x 1.1 arcsec, the mirror PSF is covered by 15 pixels half energy width of 15 arcsec. There are 600 x 600 pixels in the imaging section. In order to have CCDs orthogonal the MOS cameras are set on the spacecraft focal plane bulkhead, which means cameras cover the 300 micron gaps between the outer CCDs of each other.

The pn camera on the other hand, has twelve 3 x 1 cm pn-CCDs [60]. The four of the quadrants have three subunits of pn-CCD each having parallel operated 200 x 64 pixels. The mirror PSF has 6 x 6 cm imaging area which covers approximately 97% of the FOV and it is suitable for background studies.

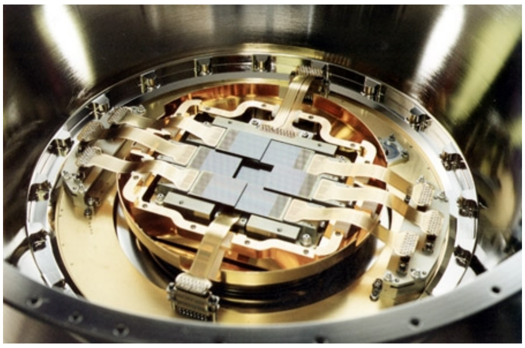

Figure 1.13. An image of MOS camera.

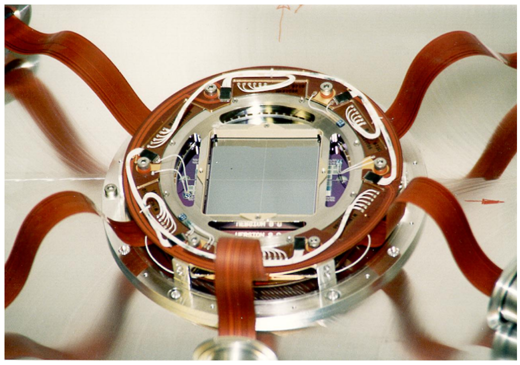

Figure 1.14. An image of pn camera.

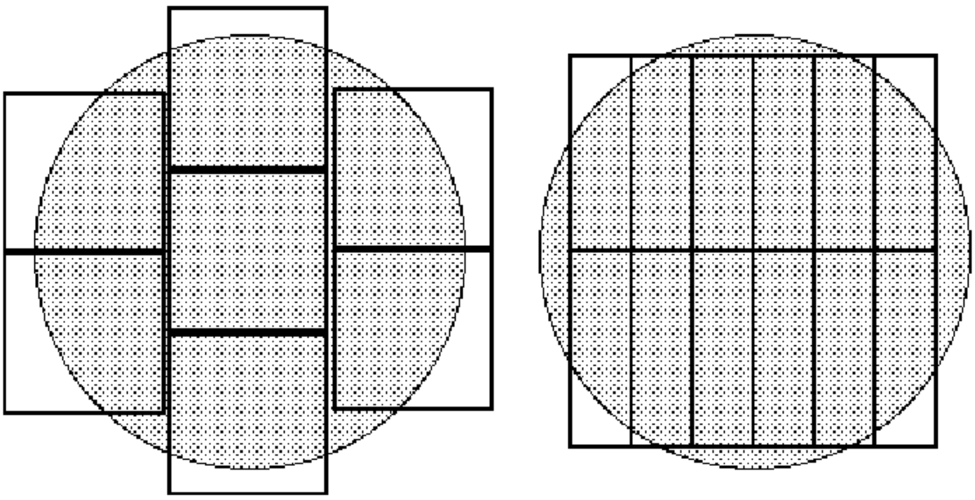

Figure 1.15. The field of view of EPIC cameras. MOS (left) having 7 CCDs each 10.9 x 10.9 arcminutes and pn (right) having 12 CCDs each 13.6 x 4.4 arcmin. The shaded circle depicts a 30′ diameter area. Credit: [63]

2. TOOTHBRUSH GALAXY CLUSTER

1RXS J0603.3+4214 was discovered[9] in 2012. It is a merging cluster at z=0.225 in which a gigantic radio halo and three radio relics appear [9]. Among the relics, the northern one is the largest with a length of 1.9 Mpc. Its morphology is a rather interesting one, it has a broader part to the west, which causes its nickname the Toothbrush. Other two relics of Toothbrush have lengths of 900 and 200 kpc approximately. They are placed east and south-east of the cluster [9]

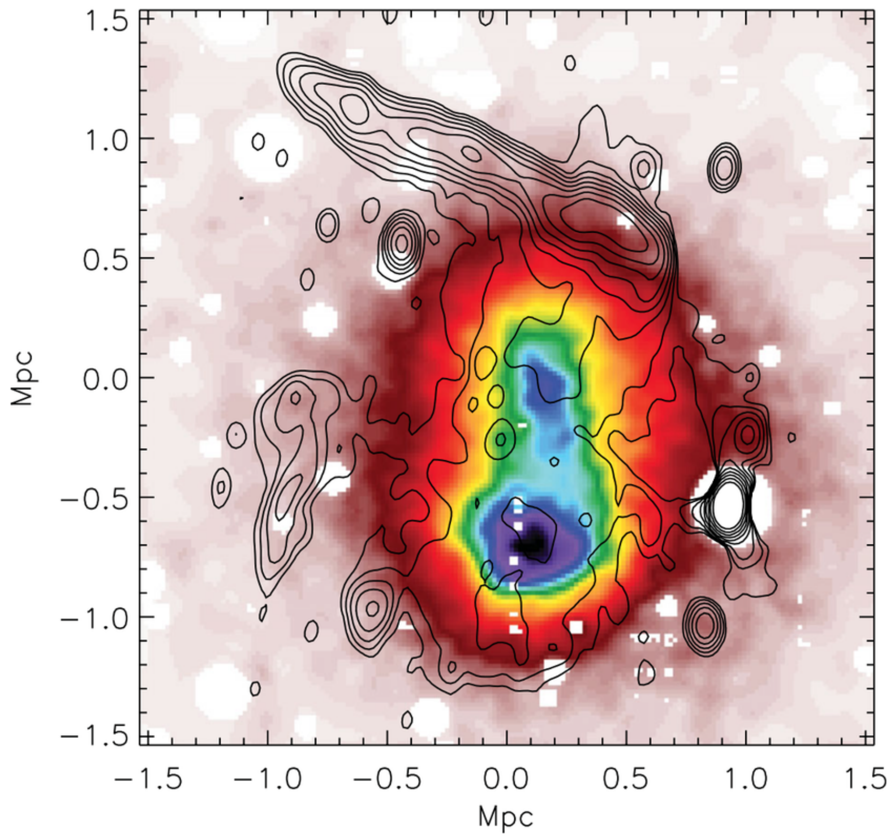

Figure 2.1. Adaptively smoothed X-ray image of the Toothbrush with WSRT L-band 1.2 - 1.8 GHz contours. Credit: [64]

2.1. Simulations of Mergers in the Toothbrush Cluster

Toothbrush cluster experienced merger that caused travelling shock waves travelling through the ICM. These shocks accelerate electrons in the ICM, and by investigating and simulating the emissions, the structure of the shocks and the mergers are studied.

Toothbrush merger is simulated[65] in order to determine the morphology of the radio relic. Their simulations show that cluster is formed by merging of three different clusters. Initially cluster 1 and 2 have a relative velocity of 1500km/s and collide each other at approximately 1.3 Gyr after simulation started. As they collide, they created an ellipsoidal shock front which is strongest along the axis of the merger. At the same time, cluster 3 touches cluster 2 loses some of its gas to cluster 2. While the cluster 3 leads to north, gravity of cluster 1 pulls cluster 3. Before colliding, it moves in an arc-shaped orbit. Once it collides with merged cluster 1 and 2, it boosts the temperature of the ICM. In fact, the hottest regions of the merged cluster are found in the region of cluster 3. Then, this hot gas creates a shock that is the strongest in the region. Simulations [65] provide evidence that the Toothbrush cluster is formed by a triple merger of clusters.

2.2. Star Formation in Toothbrush Cluster

Shock waves travel inside the ICM and it inter acts dark matter, galaxies and ICM gas since the subclusters merged. Therefore shock waves heat every available intergalactic gas inside the medium. Furthermore, it increases turbulence and causes instabilities inside the gas [66]. The disturbed gas then eventually collapses into separate clouds. These clouds that are formed because of the turbulence that shock caused, are very dense. Their density allows star formation to initiate. In 1989, M. J. Rees proposed[67] that powerful radio jets initiate star formation (SF) along their propagation axis. Although some radio jets cause stars to form, radio jets with higher Mach number do the opposite. Radio jets with very high Mach numbers (10 to 100) have too much power to let intergalactic gas to form clouds. These powerful jets sweep away the gas and form shells around star forming clumps [68]. For the Toothbrush, however, this is not the case. The cluster has shock wave with Mach numbers of at most 4[9].

It is speculated[66], that shocks with low Mach number, may have more chance of not sweeping the gas away from the galaxy, but increasing the turbulence. The increased chance of creating turbulence in the gas leads to higher chance for clouds to form and therefore increased chance of SF. In summary, a shock might help star forming clouds to originate however if the shock is too fast, it sweeps the gas so much that gas cannot form star forming clouds.

Simulations [69] show that after a radio shock passes ICM, SF lasts for 100 Myr with an error of approximately 10 Myr and new born stars trail the direction of the passed shock. The SF process, however does not strictly occur after the shock has passed. SF does not particularly happen for a small time interval, multiple episodes of SF might occur, which leads a gradient of ages.

Turbulence is initiated quickly, so is the collapsing and cooling process. Although most of the gas is used to fuel SF, some of it is thrown away from the galaxy. The removed part of the gas is mostly located at the outer disc of the galaxy cloud. The gas inside the far parts of the galaxy cloud can easily be thrown away by the shock. The shock, therefore, is expected to lead to a increase in SF for 10-100 Myr. After that period, galaxy will have a fast quenching and decrease of SF.

Analyzed effects of the merger turbulence is presented in the following sections.

3. OBSERVATION AND DATA REDUCTION

In order to investigate the abundance and temperature profile in the hot gas of Toothbrush cluster and understand how merging and shock waves affect those profiles, we need to analyze the data obtained from the XMM-Newton. The process is as the following; downloading the OBS data from archive, executing data reduction with Science Analysis System (SAS) v17.0.0 with the calibration files by June 2018 and creating regions in order to have a better understanding of abundance and temperature shift along the collision axis. Then finally by using X-Ray Spectral Fitting Package (XSPEC) version 12.10.1, fitting the extracted spectra according to the models we choose, which gives us the desired parameters.

3.1. Observation

The Toothbrush cluster was observed on 2011 October 3 and 4 (Table 3.1.). The total exposure time is 82 ks and the medium filter is used [64].

Table 3.1. Observation information of the cluster RX J0603.3+4214 at z=0.225. Data is taken from the XMM-Newton archive.

OBS ID	Target	Start Date	End Date
0675060101	+42d 12' 31.0"	2011-10-03 10:44:25	2011-10-04 10:23:55

Duration	RA	DEC	Exposures
85170	J060313.4+421231	06h 03m 13.39s	~EPIC, 11 OM, 2 RGS

3.2. Data Reduction and Image Analysis

The following information mostly depends on the XMM-ESAS Cookbook[63].

The raw XMM-Newton archive files of the Toothbrush are in Observation Data Files (ODF) format. After downloading the OBS file of the observation in TABLE, we start the data reduction process with SAS v17.0. SAS is a software to process the data collected by the XMM-Newton Observatory. At the very beginning, we create an index file known as CCF Index File (CIF) for Current Calibration File (CCF) according to our observation time and date in order to give a correct pathway to Calibration Access Layer (CAL) in the set of correct CCF with *cifbuild*. Then *odfingest* looks all ODFs and generates a summary file: the SAS ODF Summary File (*.SAS file) in terms of exposures of the observation.

Among the packages available in SAS, we choose to use the XMM-Newton Extended Source Analysis Software, XMM-ESAS since it fits our investigation of the extended source that is the galaxy cluster. It mainly used to 1) measure, create and remove non-cosmic background noises, 2) reduce extended diffuse data in a more automated way since it calls various SAS tasks in a single one, 3) create mosaic images of extended emission such as background and exposure.

For the next step, event list files (one per instrument, exposure and per mode) are created by *emchain* and *epchain* for MOS cameras and pn camera respectively. The tasks $pn - filter$ and $mos - filter$ takes the imaging exposures that previously processed by epchain and emchain, filter the data and create assorted diagnostic files. We now have our first images which can be seen in Figure 3.1.. Notice that they are not aligned or cleaned from point sources at this step. Also in the image of MOS1, it can be seen that CCD 6 is not working. The reason behind it is that a meteorite had hit CCD 6 before our observation start.

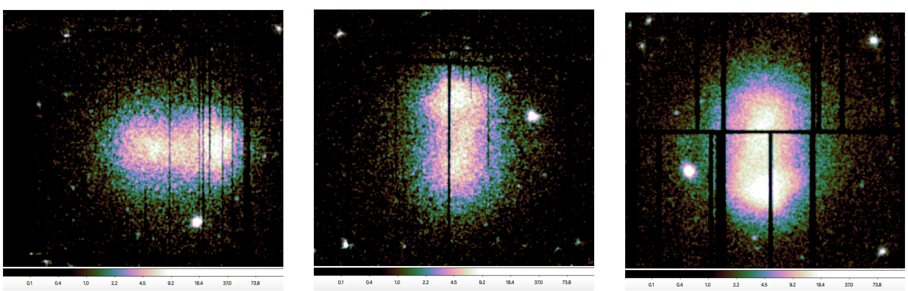

Figure 3.1. MOS1 (left), MOS2 (middle) and pn (right) filtered images.

The point source detection is performed by *cheese*. It executes SAS task *edetect_chain* and create masks which are used later to create clean spectra. The generated masks can be seen in Figure 3.2.

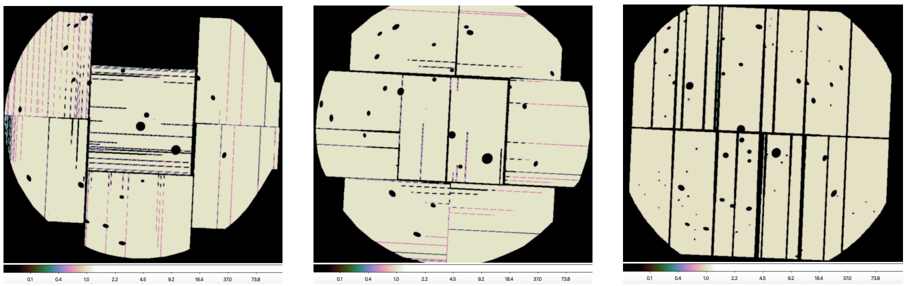

Figure 3.2. MOS1 (left), MOS2 (middle) and pn (right) cheese masks.

In order to have cleaned event files for a desired energy interval we use the tasks *mos_spectra* and *pn_spectra*. They take previously generated masks then clean the spectra. In this part 11 different regions are created along the collision axis. Every single region is generated for each camera in Figure 3.3.. Spectroscopy of each region is done simultaneously for the data from three cameras. For imaging purposes, we also used this task without masking. Quiescent particle background (QPB) spectra and images in detector coordinates are later generated by the tasks *mos_back* and *pn_back* . In order to transform these QPB images and spectra from detector coordinates to sky coordinates we execute $rot - im - det - sky$. To have a combined and smoothed image which can be seen in Figure 3.4. we use *comb* and *adapt* respectively.

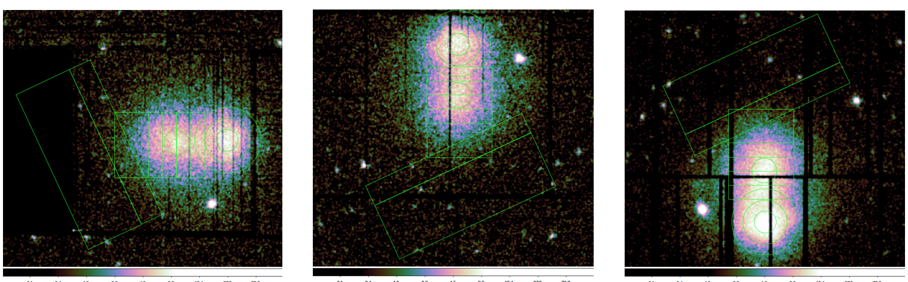

Figure 3.3. MOS1 (left), MOS2 (middle) and pn (right) region selection.

These regions are chosen in order to have the clearest possible distribution. For imaging purposes adapted image with regions selected is also created (Figure 3.5.). The south core is coloured in red and the north core is coloured in blue. There are 2 annuli encircling the south core. Some arbitrary upper part of the annuli (Region 1) is cut down by Region 4 in order to make it easy to see how the abundance and the temperature distributed along the axis. Similarly, north core (Region 6) is subtracted in the Regions 5 and 6. Half of the Region 9 seen in Figure 3.5. is cut in half by Region 10 making it a rectangle between Regions 8 and 10.

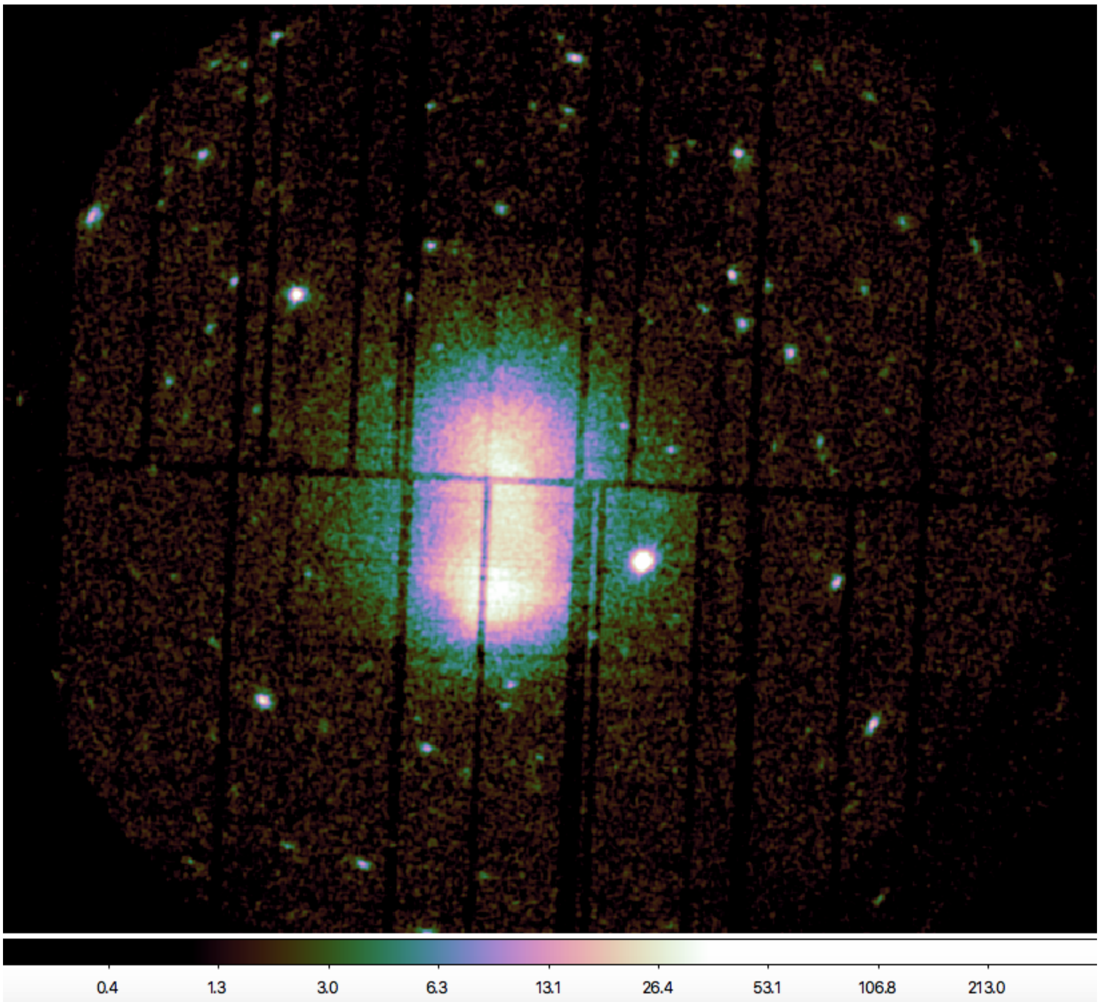

Figure 3.4. The Combined EPIC image of the Toothbrush cluster. The energy range is 0.4-12 keV.

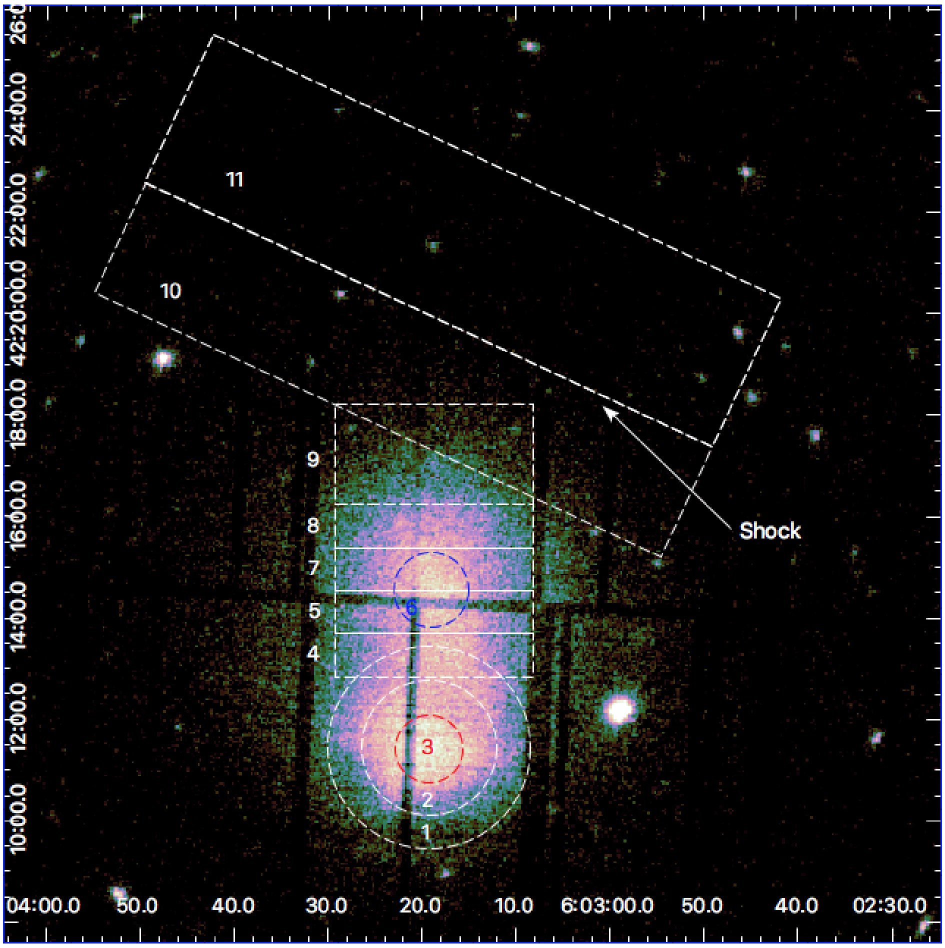

Figure 3.5. EPIC image of the Toothbrush cluster. The energy range is 0.4-12 keV. The dashed lines show the regions we investigated for spectroscopy.

3.3. Spectral Analysis

Spectral fitting is performed with X-Ray Spectral Fitting Package (XSPEC). We add appropriate models to spectra in order to describe best fit parameters. For spectral fitting we use *apec*, *phabs* and occasionally *powerlaw* if it improved the reduced χ^2 value. The background modeling, on the other hand, required *apec*, *powerlaw*, *phabs* and *gaussian*. The models are explained in this section while the actual modeling the spectra and background of the galaxy cluster is explained in the following sections.

The model APEC is used to calculate the collisionally-ionized diffuse gas by using AtomDB atomic database. It describes the emission mechanisms from the hot gas, Bremmstrehlung and line emissions in our case (look up AtomDB database[70] for detailed information). Briefly, APEC takes the distance (redshift) and gives the abundance and temperature parameter. Its normalization factor is the emission measure of the gas scaled by the distance (in cm^{-5}) and it is given by,

$$\frac{10^{14}}{4\pi[D_A(1+z)]^2}\int n_e n_H dV \tag{3.1}$$

where D_A is the angular diameter distance to the source, n_e is the electron density and n_H is the hydrogen density.

This model would provide a good fit for the spectra if the Toothbrush cluster would not be at z=0.225. The emitted photons travel many distances and get absorbed by the hydrogen cloud that surrounds the Universe. In our galaxy, the hydrogen cloud is even denser and our observation is affected by that. In order to take this absorption into account, we must add an PHABS model as a multiplication of APEC. Multiplication can be thought as a link of two models. An arbitrary photon coming to the XMM-Newton satellite is emitted by the hot ICM, and it is absorbed by the hydrogen cloud.

Therefore, we need an absorbed emission model. PHABS is given as,

$$exp[-n_H \sigma(E)] \tag{3.2}$$

where n_H is the hydrogen column density while $\sigma(E)$ is the photo-electric absorption cross-section.

POWERLAW is another model that we use. It is simply a photon power law which is given as,

$$KE^{-\alpha} \tag{3.3}$$

where K is the normalization (photons/keV/cm^2/s at 1 keV and α is the dimensionless photon index of power law.

The last model we use in our analysis is GAUSSIAN. For a desired energy band it adds gaussian line profiles as,

$$K \frac{1}{\sigma * \sqrt{2 * \pi}} \exp\left(\frac{-(E - E_l)^2}{2\sigma^2}\right) \tag{3.4}$$

where E_l is the defined line energy in units of keV (where 1eV $= 1.6 \times 10^{-12}$ ergs$=$ 1.6×10^{-19} Joule $=$ 11,605 Kelvin degrees) while σ is the line width in keV. K is the normalization as in POWERLAW.

Together with the above mentioned spectral models one can perform spectral analysis and this will be given below.

The hot ICM gas of Toothbrush cluster emits X-ray spectrum that can be modeled. We use apec model for our fits and we use this model with the addition of phabs since it is absorbed by the surrounding hydrogen cloud.

It gives,

$$phabs * apec_{spectral} \tag{3.5}$$

XMM-Newton is affected by four cosmic backgrounds that will be explained briefly in this section; Local Hot Bubble, cooler halo, hotter halo and intergalactic medium. Also, CCDs in MOS and pn cameras have specific emission lines that requires modelling.

XMM-Newton orbits around the Earth and therefore it is vulnerable to any cosmic emission. The background emission should be identified and modelled accordingly. Cosmic background consists of four components, i) Local Hot Bubble, ii) Cooler Halo, iii)Hotter Halo and iv) Unresolved Sources of Cosmic Background

The Local Hot Bubble (LHB) is a 200pc[71] region in the Orion Arm of the Milky Way, in which Solar System lies in. This hot interstellar plasma of low density, ($10^6 K 10^{-2} cm^{-3}$[71]) is probably came into existence similar to the ICM, but in smaller scale. Supernovae explosions created and enriched the Local Hot Bubble approximately 10^6 years ago. The hydrogen column density of the interstellar medium (ISM) cannot absorb the emission from LHB, therefore in order to model this background an unabsorbed thermal model is needed,

$$S_{LHB} = apec \tag{3.6}$$

having the temperature fixed to 0.1 keV [63]. The abundance of this model is set to 1.0 $Z_{\odot}$ since LHB is inside our galaxy. Similarly, redshift is fixed at 0.0.

Inside the LHB, there lies Milky Way with its galactic halo (Milky Way Halo - MWH). The almost spherical Galactic halo surrounds the Milky Way, while LHB surrounds a part of the Orion Arm.

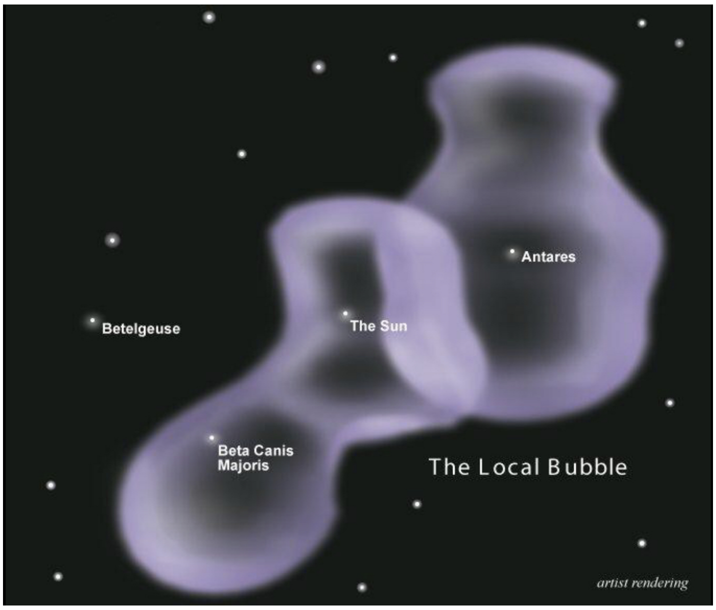

Figure 3.6. Illustrative map of the Local Hot Bubble Credit: NASA

One of the ingredients of GH is old Population II stars and globular clusters which are nearly one percent of the galaxy's stellar mass and there is no active star formation.

Apart from the stellar components, there is the galactic corona, an X-ray emitting gas extended widely.

Figure 3.7. The massive distant galaxy NGC 5746 and its halo. Credit: NASA

We need to consider the X-ray emission in order to have reasonable best fit parameters. First we model a cool absorbed thermal component with $E \sim 0.1keV$ for the cooler halo. This model, however, becomes rather ineffective since the Galactic column density of the Toothbrush cluster is dense enough (larger than $10^{20} HIcm^{-2}$) to eliminate it.

The hotter halo, on the other hand, creates absorbed thermal emission with a temperature of $E \sim 0.25 \sim 0.70 keV$ that needs to be modelled carefully. We therefore add the model,

$$S_{MWH} = phabs * apec \tag{3.7}$$

for both emissions, which results in a very low normalization for the cooler halo since it is relatively unimportant. Notice that the components are absorbed since the photons from GH travel more distance comparing that of LHB.

Third component is the unresolved background of cosmological sources. In order to model this we add,

$$S_{CS} = phabs * powerlaw \tag{3.8}$$

having $\alpha \sim 1.46$. Having the total cosmic background model,

$$apec_{LHB} + phabs * (apec_{MWH} + powerlar_{cs}) \tag{3.9}$$

Apart from the cosmological background, which is simply considering what happens to an emitted photon as it travels to our detector, there are also instrumental noise that needs to be taken care of. These instrumental backgrounds are because of the interaction of particles with the structure surrounding the detectors.

There are Al Kα and Si Kα lines for the MOS and Al Kα and Cu Kα lines for the pn that need to be modeled. In order to do so, Gaussian lines should be added at $E \sim 8.05$ keV and $E \sim 1.75$ keV for MOS; $E \sim 1.49$ keV, $E \sim 7.49$ keV, $E \sim 7.11$ keV, $E \sim 8.05$ keV, $E \sim 8.62$ keV and $E \sim 8.90$ keV to pn.

Now we have the total background model of,

$$
\begin{aligned}
&apec_{LHB} + phabs * (apec_{MWH} + powerlar_{cs}) + gaussian_{MOS:1.75} \\
&+ gaussian_{MOS:8.05} + gaussian_{pn:1.75} + gaussian_{pn:1.49} + gaussian_{pn:7.49} \\
&+ gaussian_{pn:7.11} + gaussian_{pn:8.05} + gaussian_{pn:8.62} + gaussian_{pn:8.90}
\end{aligned} \tag{3.10}
$$

4. RESULTS

4.1. Temperature and Fe Abundance Distribution Along the Collision Axis

We carefully model the spectra and background using what we have described in the previous section. The total model becomes,

$$
\begin{aligned}
&constant * [(phabs * apec_{Spectra}) \\
&+ apec_{LHB} + phabs * (apec_{MWH} + powerlar_{cs})] + gaussian_{MOS:1.75} \\
&+ gaussian_{MOS:8.05} + gaussian_{pn:1.75} + gaussian_{pn:1.49} + gaussian_{pn:7.49} \\
&+ gaussian_{pn:7.11} + gaussian_{pn:8.05} + gaussian_{pn:8.62} + gaussian_{pn:8.90}
\end{aligned}
\tag{4.1}
$$

The *constant* is a mere adjustment constant that scales the different effective areas of MOS1, MOS2 and pn. Chi-statistic is used. The parameter n_H is left free however constrained in an arbitrary interval to prevent it to give non-physical results. When it improves, a powerlaw model with low normalization is added between the first spectral apec in order to model the galactic emissions (not ICM). The general result is presented in Table 4.12.

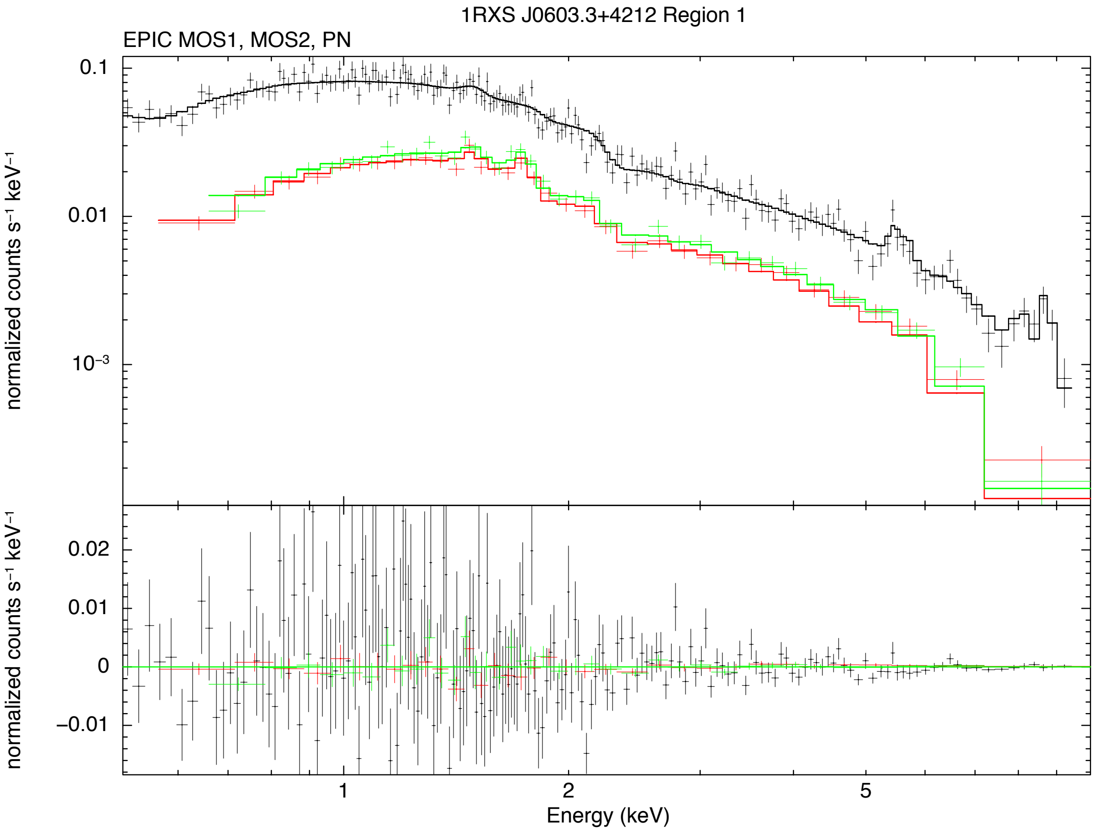

Figure 4.1. EPIC spectra of the first region of the Toothbrush cluster.

Table 4.1. Best-fit parameters for region 1.

Region 1		
kT (keV)	Abundance ($Z_\odot$)	χ^2 /d.o.f.
$9.505^{+0.781}_{-0.794}$	$0.293^{+0.122}_{-0.119}$	239/219

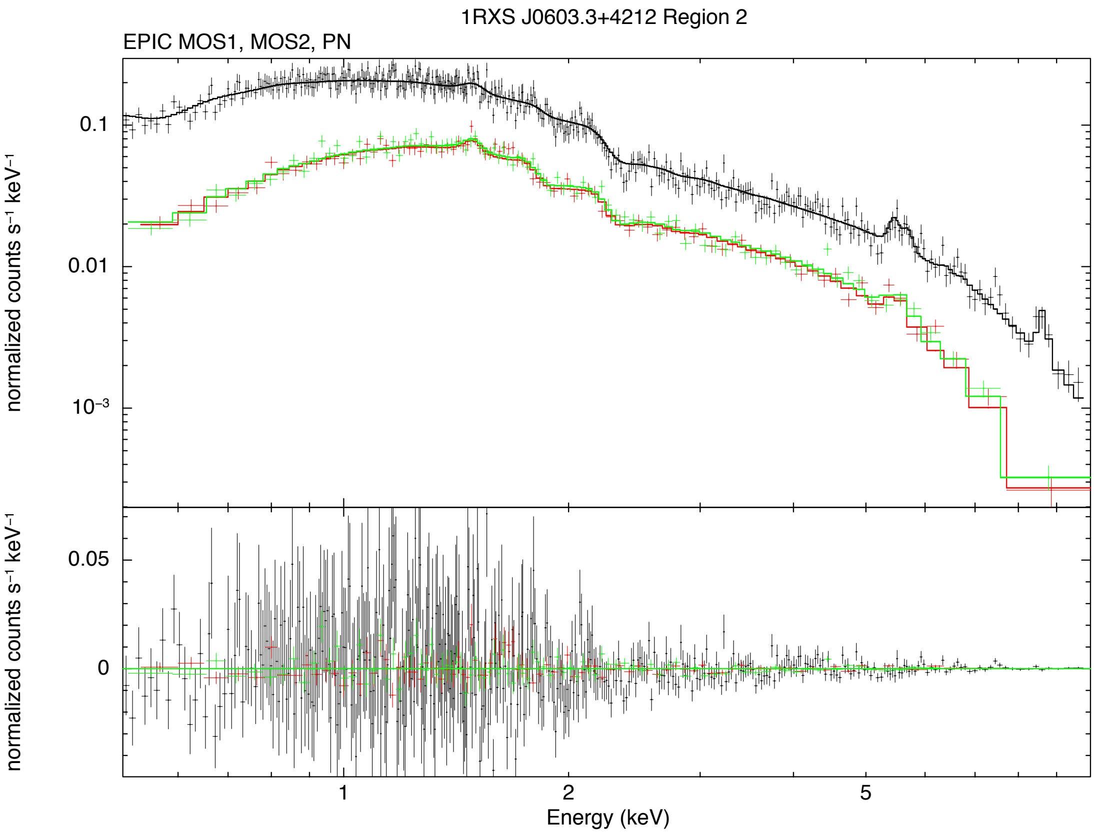

Figure 4.2. EPIC spectra of the second region of the Toothbrush cluster.

Table 4.2. Best-fit parameters for region 2.

Region 2		
kT (keV)	Abundance ($Z_\odot$)	χ^2 /d.o.f.
$9.500^{+0.423}_{-0.419}$	$0.278^{+0.061}_{-0.059}$	605/561

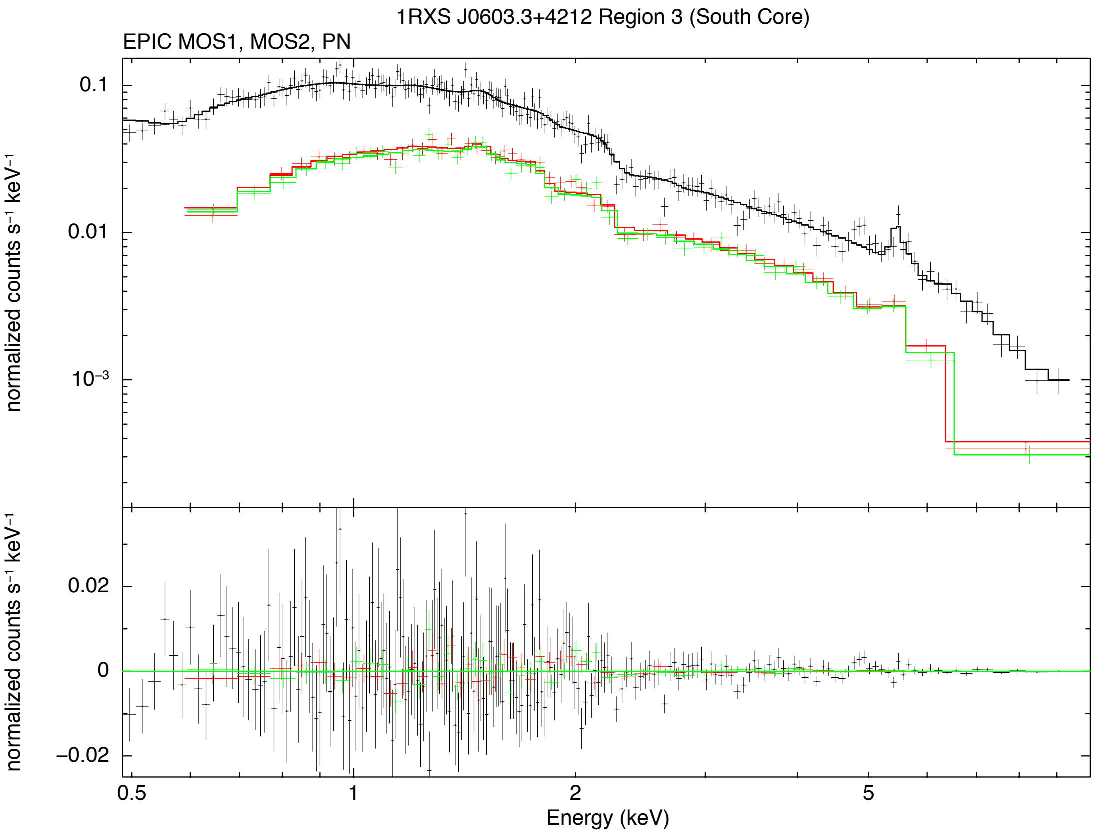

Figure 4.3. EPIC spectra of the third region of the Toothbrush cluster.

Table 4.3. Best-fit parameters for region 3.

Region 3 (South Core)		
kT (keV)	Abundance ($Z_\odot$)	χ^2 /d.o.f.
$6.000^{+0.986}_{-1.089}$	$0.303^{+0.092}_{-0.083}$	260/260

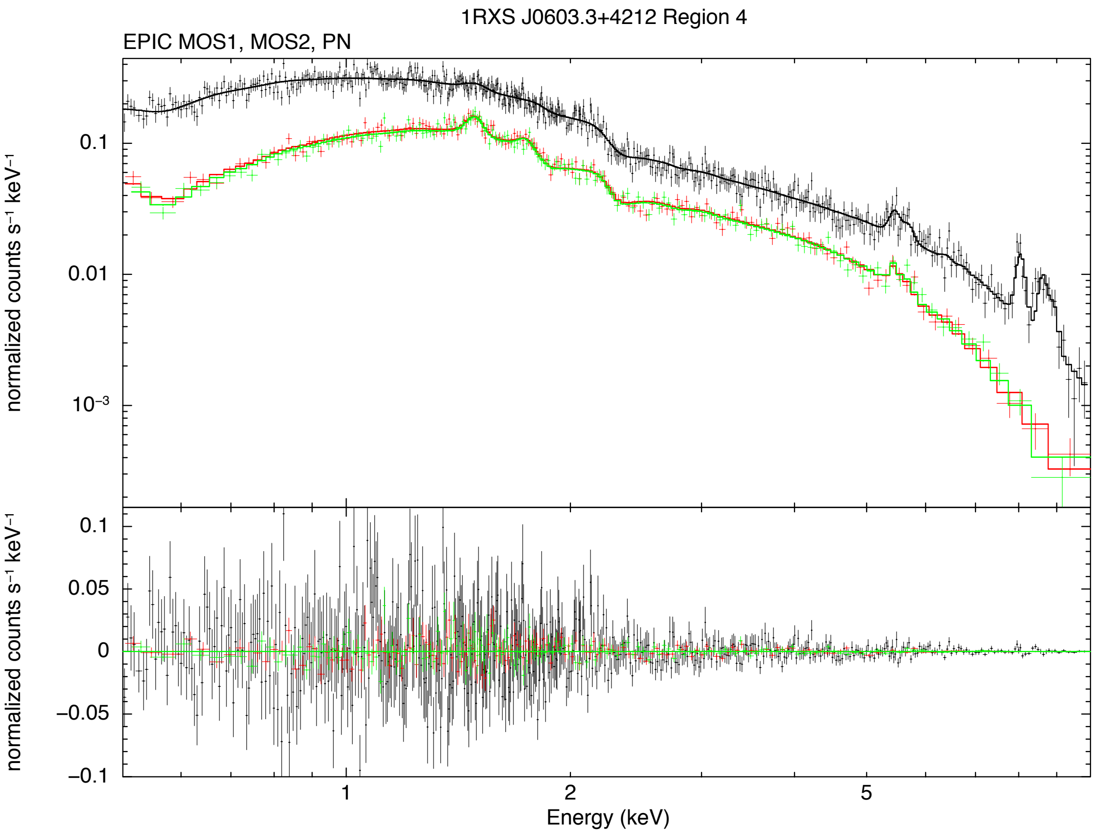

Figure 4.4. EPIC spectra of the fourth region of the Toothbrush cluster.

Table 4.4. Best-fit parameters for region 4.

Region 4		
kT (keV)	Abundance ($Z_\odot$)	χ^2 /d.o.f.
$8.445^{+0.353}_{-0.307}$	$0.225^{+0.046}_{-0.045}$	867/845

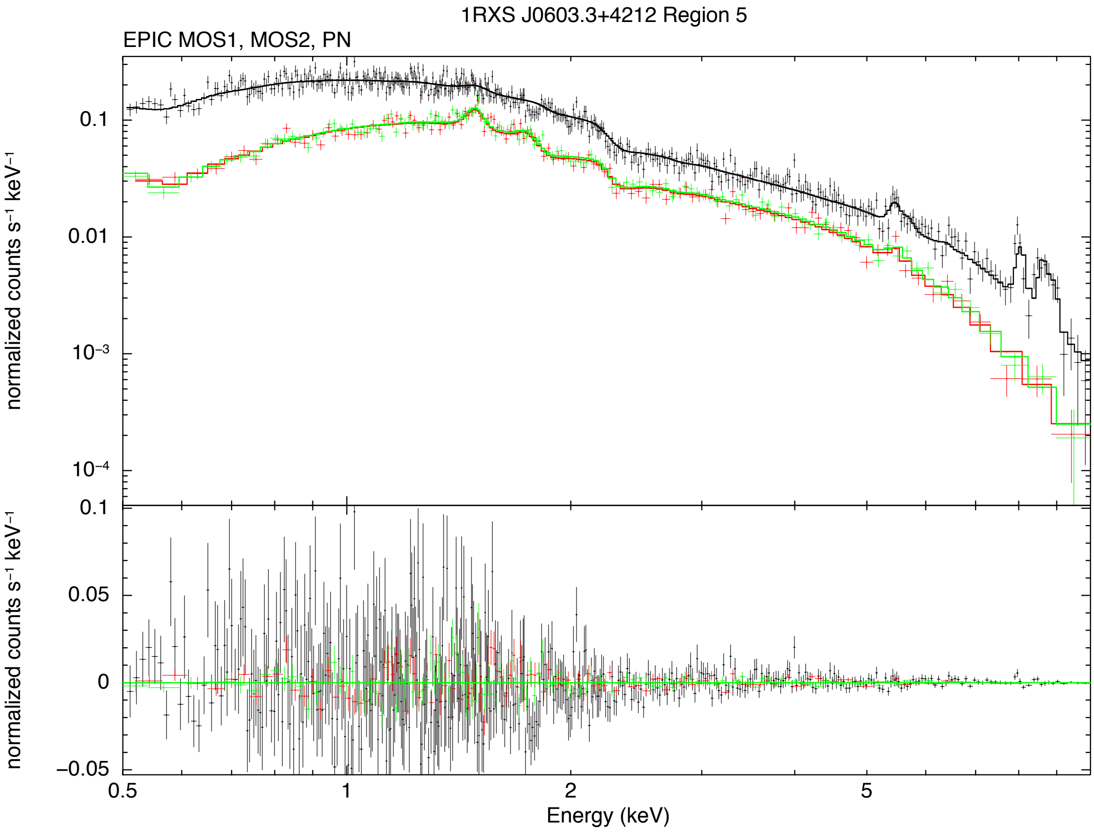

Figure 4.5. EPIC spectra of the fifth core of the Toothbrush cluster.

Table 4.5. Best-fit parameters for region 5.

Region 5		
kT (keV)	Abundance ($Z_\odot$)	χ^2 /d.o.f.
$7.638^{+0.382}_{-0.380}$	$0.178^{+0.054}_{-0.052}$	755/647

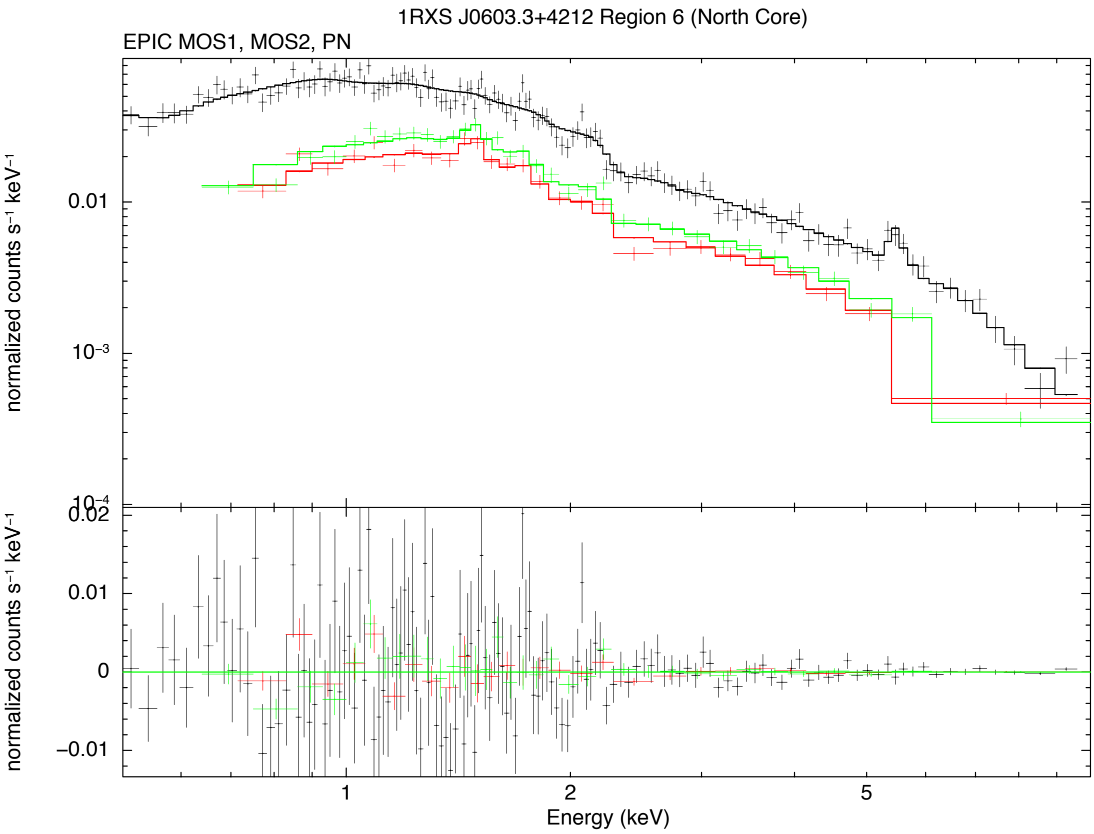

Figure 4.6. EPIC spectra of the sixth region of the Toothbrush cluster.

Table 4.6. Best-fit parameters for region 6.

Region 6 (North Core)		
kT (keV)	Abundance ($Z_{\odot}$)	χ^2 /d.o.f.
$5.630^{+1.134}_{-0.960}$	$0.366^{+0.165}_{-0.143}$	196/155

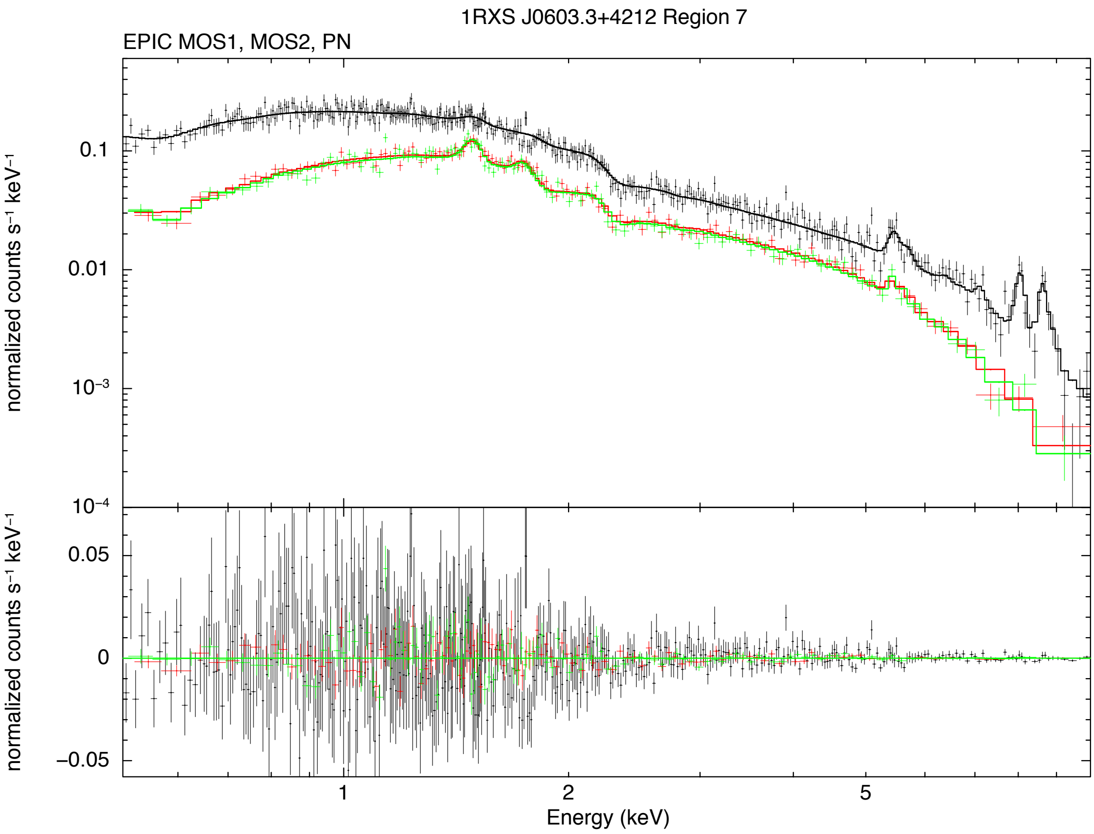

Figure 4.7. EPIC spectra of the seventh region of the Toothbrush cluster.

Table 4.7. Best-fit parameters for region 7.

Region 7		
kT (keV)	Abundance ($Z_{\odot}$)	χ^2 /d.o.f.
$7.890^{+0.522}_{-0.509}$	$0.249^{+0.060}_{-0.058}$	643/632

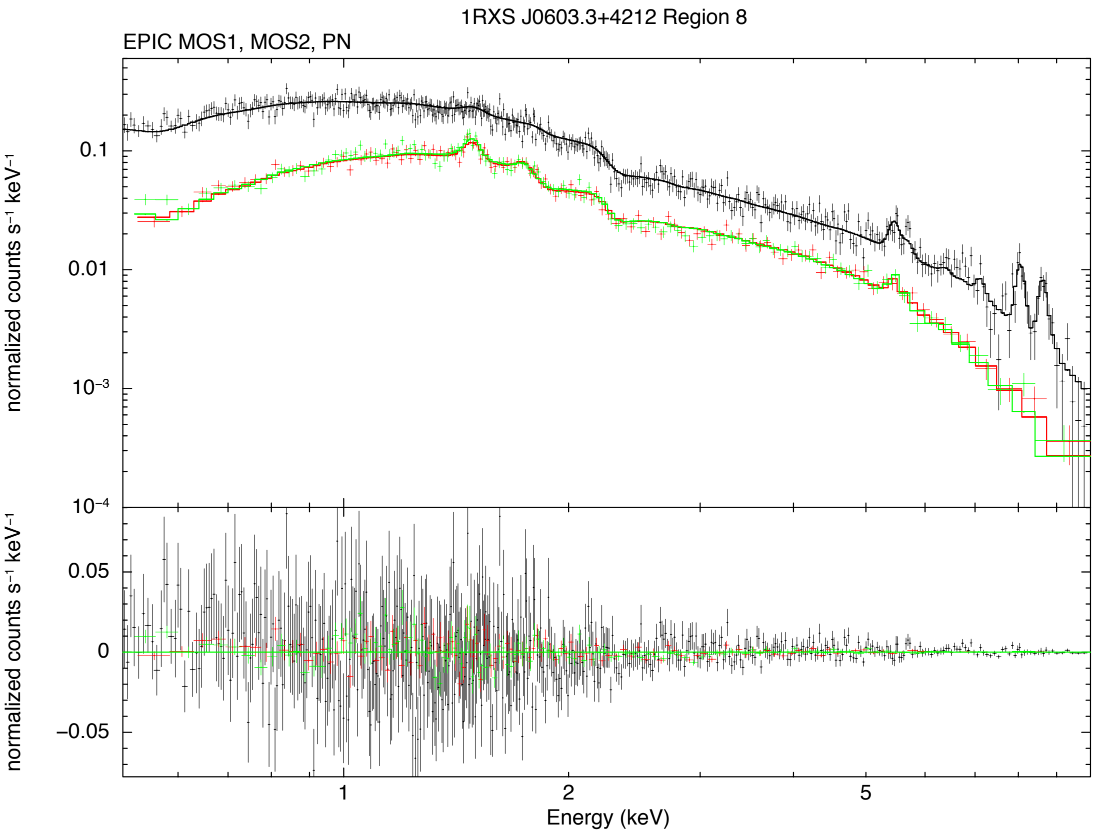

Figure 4.8. EPIC spectra of the eight region of the Toothbrush cluster.

Table 4.8. Best-fit parameters for region 8.

Region 8		
kT (keV)	Abundance ($Z_\odot$)	χ^2 /d.o.f.
$7.130^{+0.345}_{-0.340}$	$0.224^{+0.048}_{-0.047}$	754/706

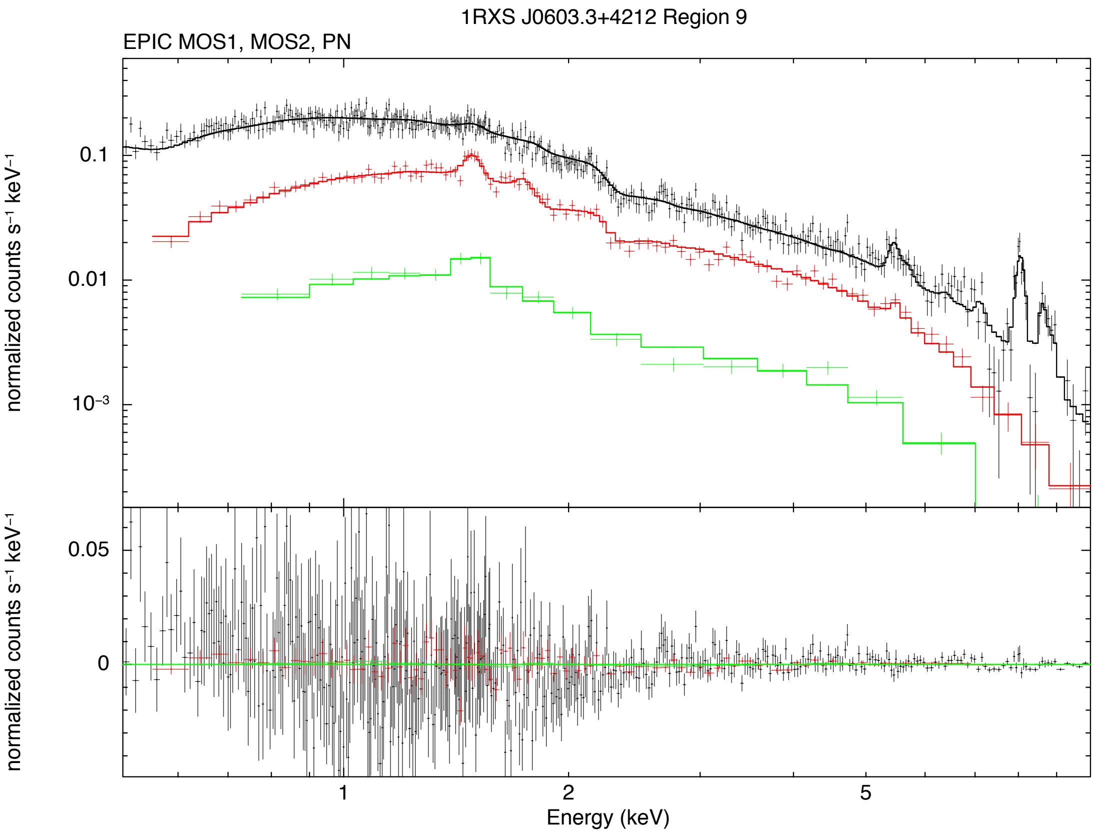

Figure 4.9. EPIC spectra of the ninth region of the Toothbrush cluster.

Table 4.9. Best-fit parameters for region 9.

Region 9		
kT (keV)	Abundance ($Z_\odot$)	χ^2 /d.o.f.
$7.034^{+0.420}_{-0.385}$	$0.231^{+0.066}_{-0.063}$	513/503

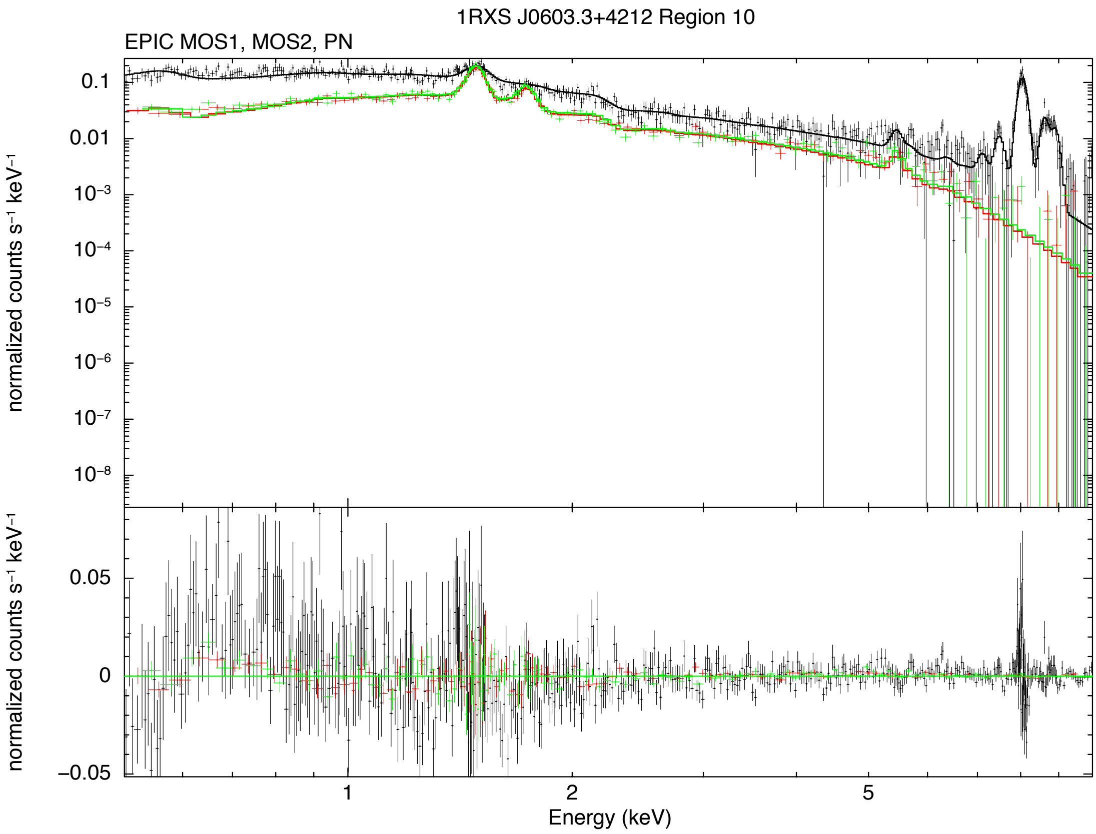

Figure 4.10. EPIC spectra of the tenth region of the Toothbrush cluster.

Table 4.10. Best-fit parameters for region 10.

Region 10		
kT (keV)	Abundance ($Z_\odot$)	χ^2 /d.o.f.
$5.512^{+0.365}_{-0.358}$	$0.255^{+0.079}_{-0.084}$	713/709

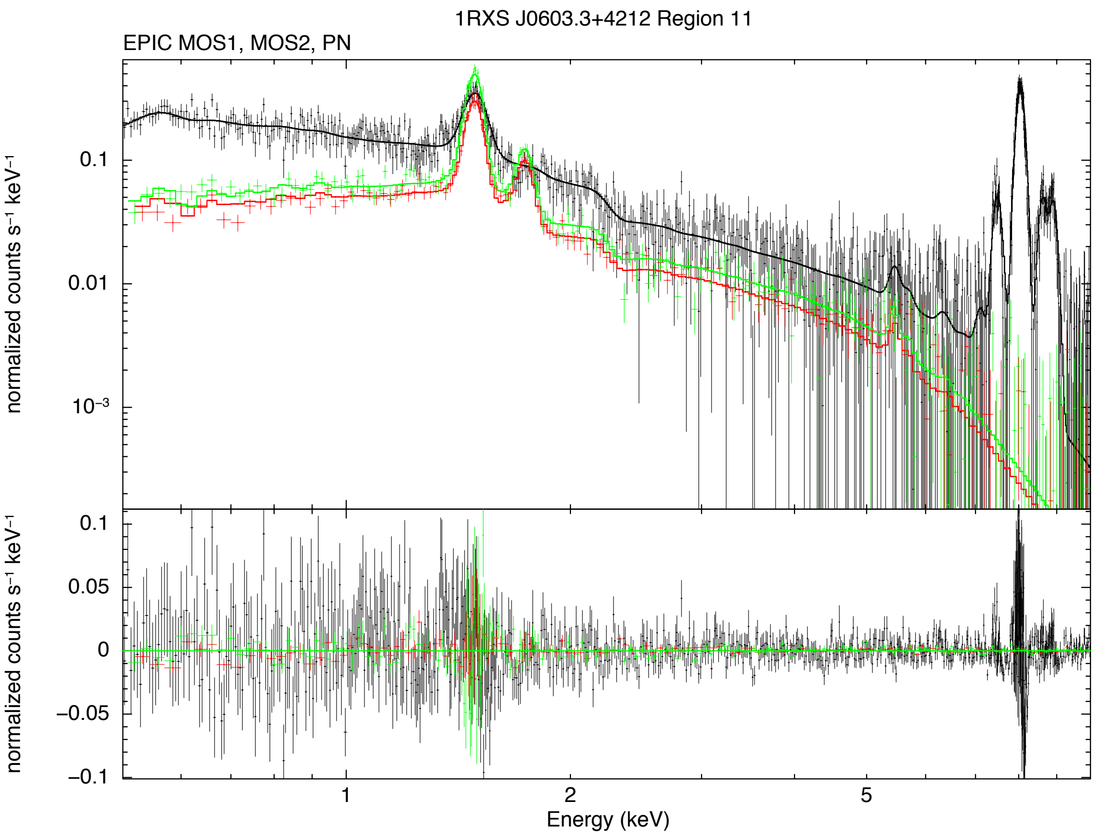

Figure 4.11. EPIC spectra of the eleventh of the Toothbrush cluster.

Table 4.11. Best-fit parameters for region 11.

Region 11 (Post Shock)		
kT (keV)	Abundance ($Z_\odot$)	χ^2 /d.o.f.
$6.759^{+0.913}_{-2.367}$	$0.256^{+0.144}_{-0.135}$	1086/1103

Table 4.12. Best-fit parameters for all regions of the Toothbrush Cluster.

Total Distribution			
Region	kT (keV)	Abundance ($Z_\odot$)	C-stat/d.o.f.
1	$9.505^{+0.781}_{-0.794}$	$0.293^{+0.122}_{-0.119}$	239/219
2	$9.500^{+0.423}_{-0.419}$	$0.278^{+0.061}_{-0.059}$	605/561
3 (CORE S)	$6.000^{+0.986}_{-1.089}$	$0.303^{+0.092}_{-0.083}$	260/260
4	$8.445^{+0.353}_{-0.307}$	$0.225^{+0.046}_{-0.045}$	867/845
5	$7.638^{+0.382}_{-0.380}$	$0.178^{+0.054}_{-0.052}$	755/647
6 (CORE N)	$5.630^{+1.134}_{-0.960}$	$0.366^{+0.165}_{-0.143}$	196/155
7	$7.890^{+0.522}_{-0.509}$	$0.249^{+0.060}_{-0.058}$	643/632
8	$7.130^{+0.345}_{-0.340}$	$0.224^{+0.048}_{-0.047}$	754/706
9	$7.034^{+0.420}_{-0.385}$	$0.231^{+0.066}_{-0.063}$	513/503
10	$5.512^{+0.365}_{-0.358}$	$0.255^{+0.079}_{-0.084}$	713/709
11	$6.759^{+0.913}_{-2.367}$	$0.256^{+0.144}_{-0.135}$	1086/1103

4.2. Discussion

As described in the previous section, we divide Toothbrush cluster to the regions and fit each of them separately and n_H left free between $0.7n_{HI} < n_H < 1.3n_{HI}$ where $n_{HI} = 2.15 \times 10^{21} cm^{-2}$[72]. The model VAPEC, which allows one to get values for each element, was tried however it is later abandoned due to the high error bars which makes it impossible to make a clear estimation about metals other than Fe. Therefore all elements are fixed to Fe. All errors are given at 2.7σ (90% confidence level).

Temperature and abundance profiles we generated (Figure 2.12.) are in a good agreement with the previous studies [64, 65]. We know that Toothbrush is a cool core and the South Core and North Core resulted as expected low temperatures of $6.000^{+0.986}_{-1.089}$ keV and $5.630^{+1.134}_{-0.960}$ keV respectively. The outer sectors of the South Core (Region number 1 and 2) are hotter with a temperature of $9.505^{+0.781}_{-0.794}$ keV and $9.500^{+0.423}_{-0.419}$ keV respectively. As we move north from the South Core, temperature begins to drop significantly. Up until to the North Core, the resulted temperatures are $8.445^{+0.353}_{-0.307}$

keV (Region number 4), $7.638^{+0.382}_{-0.380}$ keV (Region number 5). The North Core is cool as we explained, and the temperature increases slightly for the north of the North Core with a temperature of $7.890^{+0.522}_{-0.509}$ keV. Temperature does not get any hotter as we move north along the collision axis up until the shock front we have temperatures of $7.130^{+0.345}_{-0.340}$ keV, $7.034^{+0.420}_{-0.385}$ keV and $5.512^{+0.365}_{-0.358}$ keV. We can confidently say that temperature starts from the values of ~ 9.5 keV and drops to the ~ 5 keV as we move from south to the shock front. The North core and the South core deviate to this norm and spoils the smooth decrease of course, but since this is a cool-core cluster it can be an expected result. As we pass the Post-Shock sector, the result is a bit ambiguous. We have the result of $6.759^{+0.913}_{-2.367}$ keV for the Post-Shock region. Unfortunately, due

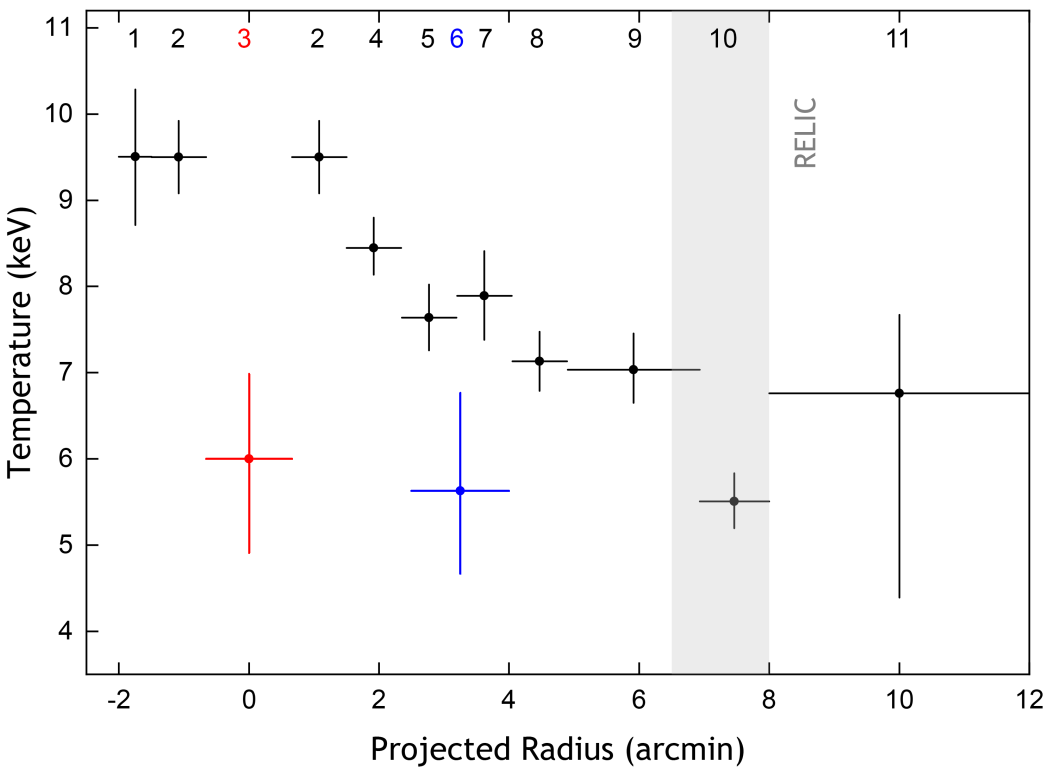

Figure 4.12. Temperature Distribution of the Toothbrush Cluster

to the high error bars, it is very hard to say anything about this region and how the shock has affected it. Clearly, the temperature might drop slightly after the shock, or jumps to the temperatures of the neighbour regions of the North Core. However, the temperature distribution is promising, it is consistent with the previous studies[64, 65] and gives very reasonable distribution along the collision axis. Simulations [65] suggest that Toothbrush had consisted of 3 clusters as explained in Section 2.1. When the cluster 3 merged the already merged 1 and 2, it created a shock (close to the south-east of the Toothbrush) that creates great turbulence and it is suggested[65] that this region may be the hottest. Our results indeed show that this sector (Region 1) is the hottest part of the cluster.

The abundance distribution is found to be rather interesting (Figure 2.13.). Our study[73] with SRON Netherlands Institute for Space Research derived abundance distribution of six merging clusters including the Toothbrush. In this study we show that there is no correlation between merging clusters on their metal abundances. Each cluster is distributed uniquely by its special merging.

Abundance profile of the Toothbrush shows rather flat one with $\sim 0.25Z_{\odot}$. The South Core has $0.303^{+0.092}_{-0.083}Z_{\odot}$ and the North Core has $0.366^{+0.165}_{-0.143}Z_{\odot}$. Intuitively in a non-merging clusters, cores are likely to have the biggest abundance. We can speculate that during the merger the abundant material is ripped from the cores and distributed accordingly. Although we must not discard the fact that cores are still very abundant, especially the North Core has more than twice average metal compared to its neighbour region. Nevertheless, the relative uniform distribution suggests that the gas belonging to the cores are disturbed and scattered. It was not able to rip the core gas entirely though. The post shock region (Region 11) again shows great error bars unfortunately. It, however, do not deviate from the relatively uniform distribution.

SF is also important since we consider shocks. As we discussed in Section 2.1, shocks below 10 Mach number help star formation by disturbing the gas and shocks above that number tear the gas and decrease the amount of SF. Since the Toothbrush has shocks $\sim$ 4 Mach number [65], shock driven SF should be considered when discussing abundance distribution. First, the shock at south-east (which is the hottest spot) lies in the Region 1 and the biggest shock relic lies in the Region 11. Unfortunately these two regions have large error bars so making an exact statement would be misleading. However it is safe to say that it is possible that metals might be more abundant in Region 1 and 11 than the "shock-free" regions that are not cores. In these regions gas might be disturbed by shocks so that SF was boosted. Therefore, as explained in Section 1.2. shocks had formed stars that must have exploded as supernovae at some portion. These explosions would enrich the ICM, which explains the increased abundance.

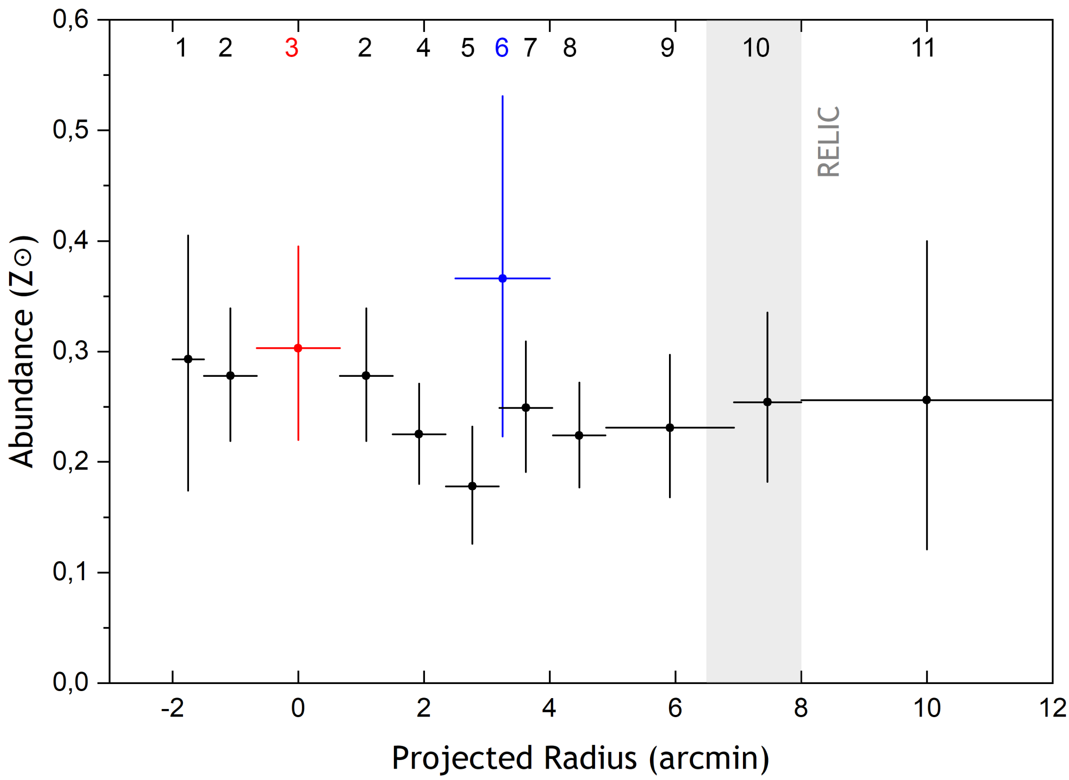

Figure 4.13. Abundance Distribution of the Toothbrush Cluster

4.3. Conclusion

In this thesis we have described the basic properties and historical background of clusters of galaxies. Later, observing the Toothbrush cluster, and clusters in general, is explained by introducing the XMM-Newton observatory. Data reduction and image analysis are explained step by step.

Galaxy clusters are the largest objects in the universe and the very massive Toothbrush cluster is an interesting one with its giant radio relics. With XSPEC we modeled and analyzed the abundance and temperature parameters. Temperature results were found to be rather expected for a cool-core cluster with cooler temperatures in cores and uniform decrease to the outskirts elsewhere, although high error bars made it impossible to deduce anything about the post shock region with confidence.

Abundance distribution, however, gave us an insight about how the shock might affected the abundant gas since metals are found to be distributed smoothly ($\sim 0.2 - 0.3$ $Z_{\odot}$). The shocks inside the cluster might scattered metals by ripping them from cores. Unfortunately, because of high error bars it is hard to make any clear statements but it can be revealed with our further studies. In order to expand this case, Chandra analysis of the cluster will be performed in the very near future. Comparing the two observational results hopefully will give us more information so that we can make clear statements. Also detecting elements individually (not as an fixed abundance) might be possible by Chandra.

REFERENCES

1. Sarazin, C. L., "Basic Properties of Clusters of Galaxies and The Physics of the Intracluster Gas", *Cambridge University Press*, February 1988.

2. Zwicky, F., *ApJ*, p. 217, 1937.

3. Voit, G. M., "Reviews of Modern Physics", *Monthly Notices of the Royal Astronomical Society*, Vol. 77, p. 207, 2005.

4. Vikhlinin, A., A. Kravtsov, W. Forman, M. M. C. Jones, S. S. Murray and L. V. Speybroeck, *ApJ*, Vol. 640, p. 691, 2006.

5. Bykov, A., E. Churazov, C. Ferrari, W. Forman, J. Kaastra, U. Klein, M. Markevitch and J. de Plaa, "Structures and components in galaxy clusters: observations and models", *Space Science Reviews*, Vol. 188, p. 141, Dec 2015.

6. Sarazin, C. L., "X-ray emissions from clusters of galaxies", *Cambridge Astrophysics Series*, 1988.

7. Matteucci, F. and F. Calura, "Early chemical enrichment of the universe and the role of very massive population III stars", *Monthly Notices of the Royal Astronomical Society*, Vol. 360, p. 447–452, 21 June 2005.

8. Werner, N. and H. Böhringer, "X-ray spectroscopy of galaxy clusters: studying astrophysical processes in the largest celestial laboratories", *The Astronomy and Astrophysics Review*, Vol. 18, pp. 127–196, February 2010.

9. van Weeren, R. J., H. J. A. Röttgering, H. T. Intema, L. Rudnick, M. Brüggen, M. Hoeft and J. B. R. Oonk, "The "toothbrush-relic": evidence for a coherent linear 2-Mpc scale shock wave in a massive merging galaxy cluster", *Astrophysics Astronomy*, Vol. 546, October 2012.

10. Messier, C., *Connaissance des Temps*, 1784.

11. Herschel, F. W., *Phil. Trans.*, Vol. 75, p. 213, 1785.

12. Flin, P., *Acta Cosmologica*, Vol. 15, p. 25, 1988.

13. d'Arrest, H., *Astr. Nachr.*, Vol. 65, p. 1, 1865.

14. Proctor, R. A., *MNRAS*, Vol. 33, p. 14, 1872.

15. Dreyer, J. L. E., *Mem. R. Astron. Soc.*, Vol. 49, p. 1, 1888.

16. Stephan, M., *MNRAS*, Vol. 37, p. 334, 1877.

17. Easton, C., *Astr. Nachr.*, Vol. 166, p. 131, 1904.

18. Reynolds, J. H., *MNRAS*, Vol. 83, p. 142, 1923.

19. Abell, G. O., "The Distribution of Rich Clusters of Galaxies", *Astrophysics Journal Supplement*, Vol. 3, p. 211, 1958.

20. Abell, G. O., *ARAA*, Vol. 3, p. 1, 1965.

21. Zwicky, F., *PASP*, Vol. 74, p. 373, 1963.

22. Baum, W. A., *PASP*, Vol. 70, p. 450, 1958.

23. Minkowki, R., *ApJ*, Vol. 132, p. 908, 1960.

24. Zwicky, F., E. Herzog, P. Wild, M. Karpowicz and C. Kowal, *Catalogue of Galaxies and Clusters of Galaxies*, 1961-1968.

25. de Vaucouleurs, G., *Galaxies and the Universe*, p. 557, 1975.

26. Tifft, W. G. and S. A. Gregory, *ApJ*, Vol. 205, p. 696, 1976.

27. Abell, G. O., *ApJ*, Vol. 213, p. 237, 1977.

28. Jôeveer, M., J. Einasto and E. Tago, *MNRAS*, Vol. 185, p. 357, 1978.

29. Einasto, J., M. Jôeveer and E. Saar, *MNRAS*, Vol. 193, p. 353, 1980.

30. Abell, G. O., *Highl. Astron.*, Vol. 6, p. 753, 1983.

31. Fabian, A. C. and P. E. J. Nulsen, "Subsonic accretion of cooling gas in clusters of galaxies", *Monthly Notices of the Royal Astronomical Society*, Vol. 180, pp. 479 – 484, 1 October 1977.

32. Fabian, A. C., “Cooling Flows in Clusters of Galaxies”, *Annu. Rev. Astron. Astrophys.*, Vol. 32, pp. 277–318, 1994.

33. Fabian, A. C., J. S. Sanders, G. B. Taylor, S. W. Allen, C. S. Crawford, R. M. Johnstone and K. Iwasawa, “A very deep Chandra observation of the Perseus cluster: shocks and ripples and conduction”, *Monthly Notices of the Royal Astronomical Society*, Vol. 366, pp. 417 – 428, 21 February 2006.

34. Sarazin, C. L., “Mergers Cosmic Rays and Nonthermal Process in Clusters of Galaxies”, *Journal of The Korean Astronomical Society*, Vol. 37, pp. 433 – 438, 2004.

35. Hoeft, M., M. Brueggen, G. Yepes, S. Gottloeber and A. Schwope, “Diffuse radio emission from clusters in the MareNostrum Universe simulation”, *MNRAS*, 8 Jul 2008.

36. Brunetti, G. and T. W. Jones, “Cosmic rays in galaxy clusters and their nonthermal emission”, *International Journal of Modern Physics D*, 29 Jan 2014.

37. Ensslin, T., P. Biermann, U. Klein and S. Kohle, “Shock Waves of the Large-Scale Structure Formation in the Universe”, Vol. 562:233-253, 29 May 1998.

38. Francesco Miniati, a. T. W. J., H. Kang and D. Ryu, “Cosmic-Ray Electrons in Groups and Clusters of Galaxies: Primary and Secondary Populations from a Numerical Cosmological Simulation”, *The Astrophysical Journal The American Astronomical Society*, July 20 2001.

39. Feretti, Luigina, Giovannini and M. Gabriele; Govoni, Federica; Murgia, “Clusters of galaxies: observational properties of the diffuse radio emission”, *The Astronomy and Astrophysics Review*, Vol. 20, May 2012.

40. Voit, G. M., “The Internal Constitution of Stars”, *Cambridge University Press*, 1926.

41. Perrin, J. B., *L’Astronomie*, Vol. 46, p. 49, 1922.

42. Bethe, H. A., “Energy Production in Stars”, *Physical Rev*, Vol. 55, p. 434, 1 March 1939.

43. Gamow, G., "Physical Review", *Physical Review*, Vol. 70, p. 572, 1946.

44. Merrill, P. W., "Spectroscopic Observations of Stars of Class", *Astrophysical Journal*, Vol. 116, p. 21, July 1952.

45. Clayton, D. D., *Principles of stellar evolution and nucleosynthesis*, University of Chicago Press, 1968.

46. Karakas, A. I., "Updated stellar yields from asymptotic giant branch models", *Monthly Notices of the Royal Astronomical Society*, Vol. 403, 11 April 2010.

47. et al, D. A. H., "The type Ia supernova SNLS-03D3bb from a super-Chandrasekhar-mass white dwarf star", *Nature*, Vol. 443, p. 308–311, 2006.

48. Riess, A. G., A. V. Filippenko, P. Challis, A. Clocchiattia, A. Diercks, P. M. Garnavich, R. L. Gilliland, C. J. Hogan, S. Jha, R. P. Kirshner, B. Leibundgut, M. M. Phillips, D. Reiss, B. P. Schmidt, R. A. Schommer, R. C. Smith, J. Spyromilio, C. Stubbs, N. B. Suntzeff and J. Tonry, "Observational Evidence from Supernovae for an Accelerating Universe and a Cosmological Constant", *Astron.J*, Vol. 116, pp. 1009 – 10038, 15 May 1998.

49. Iwamoto, K., F. Brachwitz, K. Nomoto, N. Kishimoto, H. Umeda, W. R. Hix and F.-K. Thielemann, "Nucleosynthesis in Chandrasekhar Mass Models for Type Ia Supernovae and Constraints on Progenitor Systems and Burning-Front Propagation", *The Astrophysical Journal Supplement Series*, Vol. 125, 1999.

50. Martin, D., A. Perego, A. Arcones, O. Korobkin and F.-K. Thielemann, "Nucleosynthesis in the Ejecta of Neutron Star Mergers", *APJ*, Vol. 813, p. 2, 25 Sep 2015.

51. Fryer, C. L., K. Belczynski, E. Ramirez-Ruiz, S. Rosswog, G. Shen and A. W. Steiner, "The Fate of the Compact Remnant in Neutron Star Mergers", *ApJ*, 28 Apr 2015.

52. de Plaa, J., "The origin of the chemical elements in cluster cores", *Astronomical Notes*, Vol. 334, pp. 416–421, 02 May 2013.

53. Matsumoto, H., "Discovery of an Abundance Gradient in the Central Region of the Virgo Cluster", *Publications of the Astronomical Society of Japan*, Vol. 48, pp. 201–210, April 1996.

54. de Plaa, J., "Constraining supernova models using the hot gas in clusters of galaxies", *AA*, Vol. 465, p. 345–355, 2007.

55. Bulbul, G. E., "High-Resolution XMM-Newton Spectroscopy of the Cooling Flow Cluster A3112", *The Astrophysical Journal*, Vol. 747, 2012.

56. Lee, J. and M. Baldi, "Can Coupled Dark Energy Speed Up the Bullet Cluster?", *The Astrophysical Journal*, Vol. 747, 2012.

57. Flynn, C., *University of Turku*, 15 October 2006, `http://www.astro.utu.fi/ cflynn/astroII/l3.htmlintens`, accessed in May 2019.

58. Karzas, W. J. and R. Latter, "Electron Radiative Transitions in a Coulomb Field", *The Astrophysical Journal Supplement Series*, Vol. 6, p. 167, 1961.

59. Ezer, C., *Chemical Enrichment History and Gas Mass Fraction of the Galaxy Cluster Abell 3112*, Ph.D. Thesis, Boğaziçi University, 2008.

60. Lumb, D. H., N. Schartel and F. A. Jansen, "XMM-Newton (X-Ray Mulit-Mirror Mission) Observatory", *Opt. Eng*, 8 Feb 2012.

61. et al, F. A. J., "XMM-Newton observatory I. The spacecraft and operations", *A&A*, 2000.

62. Gondoin, P., "Lithium abundance dispersion in the Pleiades and M 34", *AA*, Vol. 566, 2014.

63. Snowden, S. L., *Cookbook for Analysis Procedures for XMM-Newton EPIC Observations of Extended Objects and the Diffuse Background*, NASA, 15 April 2014.

64. Ogrean, G. A., M. Brüggen, R. J. van Weeren, H. Röttgering, J. H. Croston and M. Hoeft, "Challenges to our understanding of radio relics: X-ray observations of the Toothbrush cluster", *MNRAS*, 6 Mar 2013.

65. Bruggen, M., R. van Weeren and H. Rottgering, "Simulating the toothbrush: evidence for a triple merger of galaxy clusters", *Monthly Notices of the Royal Astronomical Society*, Vol. 425, pp. L76–L80, September 2012.

66. Stroe, A., D. Sobral, W. Dawson, M. J. Jee, H. Hoekstra, D. Wittman, R. J. van Weeren, M. Brüggen and H. J. A. Röttgering, "The rise and fall of star formation in z $\sim$ 0.2 merging galaxy clusters", *Monthly Notices of the Royal Astronomical Society*, Vol. 450, pp. 646–665, June 2015.

67. Rees, M. J., "The radio/optical alignment of high-z radio galaxies: triggering of star formation in radio lobes", *Monthly Notices of the Royal Astronomical Society*, Vol. 239, pp. 1p–4p, 01 July 1989.

68. M., C. R., *MNRAS*, Vol. 421, p. 1603, 2012.

69. Roediger, E., M. Brüggen, M. Owers, H. Ebeling and M. Sun, "Star formation in shocked cluster spirals and their tails", *Monthly Notices of the Royal Astronomical Society*, p. 1–6, 25 September 2011.

70. for Astrophysicists, A. D., 2018, `http://www.atomdb.org/index.php`, accessed in May 2019.

71. Einasto, J., M. Einasto, P. Frisch, S. Gottlober, V. Müller, V. Saar, A. A. Starobinsky, E. Tago, D. Tucker and H. Andernach, "The supercluster-void network - II. An oscillating cluster correlation function", *Monthly Notices of the Royal Astronomical Society*, Vol. 289, p. 801–812, 1997.

72. Willingale, R., R. L. C. Starling, A. P. Beardmore, N. R. Tanvir and P. T. O'Brien, "Calibration of X-ray absorption in our Galaxy", *Monthly Notices of the Royal Astronomical Society*, Vol. 431, p. 394–404, 2013.

73. Urdampilleta, I., F. Mernier, J. S. Kaastra, A. Simionescu, J. de Plaa, S. Kara and E. N. Ercan, "Iron abundance distribution in the hot gas of merging galaxy clusters", *Astronomy and Astrophysics*, 2019.